

UC San Diego

UC San Diego Electronic Theses and Dissertations

Title

Combustion Dynamics of a Laminar Premixed Flame in a Rijke Tube

Permalink

<https://escholarship.org/uc/item/1hw3x1c7>

Author

Finn, Patrick Calum

Publication Date

2022

Peer reviewed|Thesis/dissertation

UNIVERSITY OF CALIFORNIA SAN DIEGO

Combustion Dynamics of a Laminar Premixed Flame in a Rijke Tube

A thesis submitted in partial satisfaction of the
requirements for the degree Master of Science

in

Mechanical Engineering

by

Patrick Finn

Committee in charge:

Professor Abhishek Saha, Chair
Professor Boris Krämer
Professor Kalyanasundaram Seshadri

2022

Copyright

Patrick Finn, 2022

All rights reserved.

The Thesis of Patrick Finn is approved, and it is acceptable in quality and form for publication on microfilm and electronically.

University of California San Diego

2022

To my Mother and Father, for their continuous support of my education and career endeavours.

TABLE OF CONTENTS

Thesis Approval Page	iii
Table of Contents	v
List of Figures	vi
Acknowledgements	ix
Vita	x
Abstract of the Thesis	xi
Chapter 1 Introduction	1
1.1 Background	1
1.2 General Studies on Thermoacoustics.....	3
1.3 General Studies on the Rijke Tube.....	7
1.4 The goal of the present study	9
1.5 Outline of the thesis.....	10
Chapter 2 Methodology	12
2.1 Rijke Tube Experimental Setup Development	12
2.1.1 Selection of Rijke Tube Parameters	12
2.1.2 Flame Configuration	13
2.2 Multi-flame Dynamics Experimental Setup	15
Chapter 3 Results	19
3.1 Characterization of a Rijke Tube Based on Dynamics of a Single-Flame	19
3.2 A Systematic Investigation of The Affect of Multi-Flame Dynamics on Thermoacoustic Instability.....	20
3.2.1 Single Flame and Seven Flame Experiments	20
3.2.2 Linear Three Flame Experiment	22
3.2.3 Synchronization Analysis	26
3.2.4 Dynamics of the Heat Release Rate	30
3.2.5 Asymmetrical Three Flame Experiment	35
Chapter 4 Conclusion and future work	39
4.1 Conclusion	39
4.2 Future Work	40
4.3 Appendix	41
Bibliography	52

LIST OF FIGURES

Figure 1.1.	Example of a burner nozzle before damage(left) from combustion instability and after(right).	2
Figure 1.2.	The general feedback mechanism of thermoacoustic instability and how oscillations may build within the combustion chamber	4
Figure 1.3.	Diagram of a Rijke Tube	8
Figure 2.1.	General Rijke Tube Setup Diagram.	12
Figure 2.2.	Final Experimental Rijke tube setup model.	15
Figure 2.3.	Comparison of a conical flame during stable operation (left) and during thermoacoustic instability(right)	17
Figure 2.4.	Four burner tips and their respective diagrams	18
Figure 3.1.	P' bifurcation plots for the seven-flame and single-flame experiments. The seven-flame P' data was taken in 1cm intervals and the single-flame data was taken in 5cm intervals.	21
Figure 3.2.	Unfiltered image set of the single flame at 20cm.	21
Figure 3.3.	Unfiltered images of the 7H burner tip at 39cm.	22
Figure 3.4.	In-line three flame P' bifurcation plot from 0cm to 82cm in 1cm intervals.	23
Figure 3.5.	The time series(left 2 graphs), PSD(center right), and reconstructed phase space(right) of P' select locations along the Rijke tube.	24
Figure 3.6.	Continuous wavelet transform for P' of 46cm, mixed mode(left), and 59cm, burst mode(right).	26
Figure 3.7.	Phase Lock Value of P' and all three \dot{q}' for each location past the initial bifurcation point.	27
Figure 3.8.	Relative mean frequency between \dot{q}' of each flame and P' for each location.	29
Figure 3.9.	<i>PLV</i> between \dot{q}'_L , \dot{q}'_R , and \dot{q}'_C	30
Figure 3.10.	Image of the 3HL flames and how they are separated within the frame	31
Figure 3.11.	PSD's of each \dot{q}' and P' at $x = 22\text{cm}$	31
Figure 3.12.	Filtered images of the flames during fish-bone instability at 22cm.	32

Figure 3.13.	Time series of each \dot{q}' and P' at $x = 22\text{cm}$	32
Figure 3.14.	PSD's of each \dot{q}' and P' at $x = 70\text{cm}$	34
Figure 3.15.	Filtered images of the flames during limit cycle oscillations at 70cm	34
Figure 3.16.	Time series of each \dot{q}' and P' at $x = 70\text{cm}$	35
Figure 3.17.	Bifurcation plot of P' for the asymmetrical(green) and in-line(purple) burner tip experiments	36
Figure 3.18.	P' signal and PSD of the in-line(top) and asymmetrical(bottom) three flame burner experiments at 19cm in the Rijke.	37
Figure 3.19.	Steady State Flame on the 1H tip	37
Figure 3.20.	Unstable flames on the 7H tip.	37
Figure 3.21.	Unstable flames on the 3HL 3-flame tip	38
Figure 3.22.	Unstable flames on the 3HT tip	38
Figure 4.1.	Normalized P' from the 50.8 mm diameter Rijke tube	41
Figure 4.2.	PSD of P' from the 50.8mm diameter Rijke tube	42
Figure 4.3.	Background noise of the setup recorded from the bottom pressure sensor	43
Figure 4.4.	Pressure Sensor sound test setup diagram	44
Figure 4.5.	Top and Bottom Pressure Sensor Calibration Test Data	45
Figure 4.6.	Top and Bottom Pressure Sensor Calibration Test PSD's.	45
Figure 4.7.	Time series data of each \dot{q}' and P' during fish-bone instability at 22cm	46
Figure 4.8.	PSD's of each \dot{q}' and P' during fish-bone instability at 22cm	46
Figure 4.9.	Time series data of each \dot{q}' and P' during mixed-mode instability at 33cm	47
Figure 4.10.	PSD's of each \dot{q}' and P' during mixed-mode instability at 33cm	47
Figure 4.11.	Time series data of each \dot{q}' and P' during mixed-mode instability at 46cm	48
Figure 4.12.	PSD's of each \dot{q}' and P' during mixed-mode instability at 46cm	48
Figure 4.13.	Time series data of each \dot{q}' and P' during burst-mode instability at 59cm	49

Figure 4.14. PSD's of each \dot{q}' and P' during burst-mode instability at 59cm 49

Figure 4.15. Time series data of each \dot{q}' and P' during limit cycle oscillations at 70cm.. 50

Figure 4.16. PSD's of each \dot{q}' and P' during limit cycle oscillations at 70cm 50

Figure 4.17. Minimum dimensions required to prevent false trajectory crossings for each location..... 51

ACKNOWLEDGEMENTS

First and foremost, I would like to express my sincere gratitude to my advisor Prof. Abhishek Saha for his continuous support of my masters research. His guidance was invaluable, and this study would have been not have been possible without his help.

I would also like to express my gratitude to the members of my thesis committee, namely Prof. Boris Kramer, and Prof. Kalyanasundaram Seshadri, for their insightful comments, as well as encouragement to continue work within this topic of research.

Also, I would like to thank all the members of the Flame-Fluids-Energy lab for providing their expertise during my research. I thoroughly enjoyed their company throughout my time working in the lab. I am particularly grateful to Mr. Yue Weng, Mr. Aditya Potnis, and Mr. Sombuddha Bagchi for assisting me with experiments and data analyses.

Last but not least, I am grateful to my family for all the encouragement they provided throughout my time at University of California San Diego.

VITA

B. S. in Mechanical Engineering, University of California San Diego

M. S. in Mechanical Engineering, University of California San Diego

ABSTRACT OF THE THESIS

Combustion Dynamics of a Laminar Premixed Flame in a Rijke Tube

by

Patrick Finn

Master of Science in Mechanical Engineering

University of California San Diego, 2022

Professor Abhishek Saha, Chair

Thermoacoustic instability which stems from the non-linear interactions between heat release and pressure waves in a confined combustion chamber, can create large amplitude pressure oscillations. These oscillations may cause significant damage to the combustor hardware, and even surroundings. Accurate characterization and prediction of such instability is challenging due to its inherent complexities arising from the non-linear nature of the problem. In this thesis, we design a Rijke tube, a device in which self-excited thermoacoustic instabilities can be studied for relatively simple flame geometries. Subsequently, we used the Rijke tube to investigate dynamics of thermoacoustic instability in premixed laminar flame. We focused on the role of burner design on the ensuing instability and flame dynamics by investigating pressure oscillations

observed in four different single- and multi-flame burners. We observed that the single-flame burner did not display transition to an unstable state, when the burner was traversed along the length of the Rijke tube, while a seven-flame burner showed various states of instability and multiple bifurcation points. This observation confirms that the increased degree of freedom, arising from the interaction between individual flames in a multi-flame burner, is responsible for the wider dynamics observed.

Subsequently, to quantify the dynamics of individual flames and their roles in the ensuing pressure dynamics, a three flame burner, where the flames are located in-line, were studied in details. The Phase Lock Value, Root Mean Frequency, and Power Spectral Density were analyzed for the heat release rates from individual flames and the acoustic pressure. We observed that the center flame possessed stronger synchronization with the pressure. But, the left and right flames shared a few modes (frequencies) of oscillations with the pressure, that were not present in the center flame. This suggests that the dynamics that effect of the individual flames pose varying degrees of influence on the pressure dynamics.

An additional experiment was also conducted using an asymmetric three-flame burner, where the flames are located at the tip of an isosceles triangle, using the same flame conditions. This flame showed stronger pressure oscillations, perhaps due to enhanced degrees of interactions between three flames with the symmetric design, and eventually suffered blow-off. These systematic investigations highlights the strong influence of local flame interactions on the observed pressure dynamics, which is relevant for design of multi-nozzle combustors.

Chapter 1

Introduction

1.1 Background

In modern combustion devices, self-excited pressure oscillations can create large amplitude vibrations which cause unforeseen damage to the related hardware. These self-sustained oscillations of pressure and velocity occurring in reacting flows are generated by the interaction between sound waves and heat release within a chamber which is known as thermoacoustic instability [1]. Combustion-driven applications such as gas turbines [2], rocket engines [3] [4], air-breathing propulsion engines [5] and industrial furnaces [6] are very susceptible to this. Figure 1.1 shows an example of how a gas turbine combustor may be affected by instabilities during operation. Due to the high complexity of combustion systems, engineers desire to understand the dynamical behavior of thermoacoustics in order to mitigate risks and reduce operating costs.

Thermoacoustic instability has historically affected many combustion devices throughout the twentieth century. Most notable of this was the F1 rocket engine on the Saturn rockets, used during the first spaceflights to the moon, which developed high amplitude instabilities within its combustion chamber during operation [7, 8]. This caused catastrophic damage to the engines and required a costly test campaign to solve.

Combustion instability within rocket engines is not limited to liquid propellants. There has even been noted evidence of thermoacoustics within solid propellant engines as well due to the gasification of the solid fuel during operation [1]. This includes the Space Shuttle boosters as

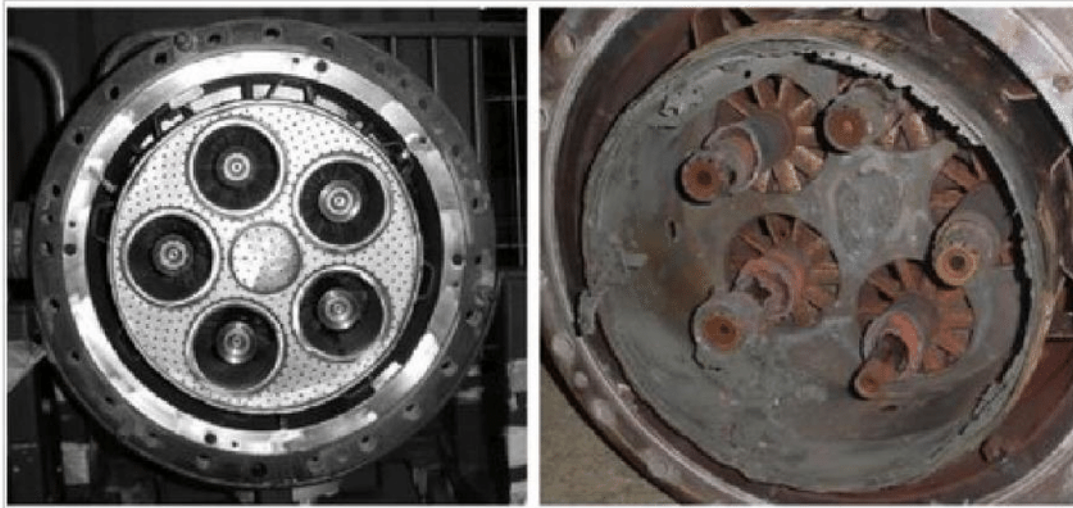


Figure 1.1. Example of a burner nozzle before damage(left) from combustion instability and after(right).

well as the Mars Pathfinder descent motors [7].

Air-breathing engines have also developed instabilities as well. One notable case being thermoacoustic instability within ramjet air intakes. Their influence on the shock system in the inlet diffuser can reduce the inlet stability margin [5]. On jet engines, afterburners will operate with reduced performance due to thermoacoustic instability. Jet aircraft afterburners are susceptible to failure or blowout due to combustion instabilities [5].

There are three well known major causes of combustion instability to the aforementioned examples. The first being low-frequency oscillations caused by interaction between propellant feed systems and combustion. This is sufficiently understood and comparatively easy to avoid by implementing preventative measures within the fuel and oxidizer feed system [4]. The second is intermediate frequency instability resulting from an entropy wave interacting with the exhaust of the nozzle or chamber [9]. The third and most critical is the high-frequency instability that is formed from the excitation of acoustic vibrational modes of the combustion chamber. This paper will focus on the third mode of instability.

1.2 General Studies on Thermoacoustics

Thermoacoustic physical phenomenon was initially observed in the late 19th century by Lord Rayleigh, citing that a sound developed when a hot glass bulb was held at the end of a glass-blowing tube [10]. This observation was caused by the fluctuating heat release amplifying the acoustic oscillations, where the acoustic pressure and unsteady heat release rate were in phase. This is now known as the Rayleigh Criterion.

A few decades later, Putnam and Dennis carried out multiple experiments with a variety of combustion devices to study thermoacoustics and the Rayleigh criterion. They verified that the acoustic pressure and unsteady heat release rate were coupled and that this state depended on the combustion chamber size relative to the velocity of the gas [11]. Their mathematical model of the Rayleigh criterion is shown in equation 1.1. The amplitude of oscillations will increase when “I” is constant. “I” is the integral of the instantaneous heat release rate multiplied by acoustic pressure perturbation over one cycle.

$$I = \int q' P' dt \quad (1.1)$$

By the 1960's Blackshear worked to improve upon the Rayleigh criterion by experimenting with a ducted flame and how it will amplify or dampen an acoustic standing wave. He concluded that when the standing wave within the flow field generated by the interaction between heat release rate and the flow velocity are in phase, they drive the standing wave. If they are opposed, the standing wave dampens. The flame conditions as well as position within the chamber will therefore affect the dynamical state of the unsteady heat release rate and the acoustic pressure. Blackshear also observed that the standing wave amplitude may increase enough to cause the flame to blow off or flash back [12]. A visual representation of how the feedback between heat release rate and perturbations within the flow is shown in figure 1.2. As noted in equation 1.1, the heat release rate and pressure will amplify or dampen the oscillations within a chamber. A few

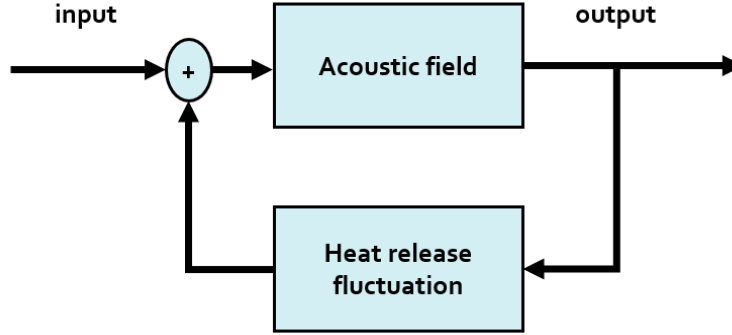


Figure 1.2. The general feedback mechanism of thermoacoustic instability and how oscillations may build within the combustion chamber

years later Crocco introduced a time-lag between acoustic pressure and unsteady heat release rate to account for the different chamber lengths and how the length affects the overall stability of the system [4]. He included the fluid dynamics model representing the small perturbations within the combustion chamber, specifically for rocket engines, as seen in the one-dimensional continuity equation 1.2 and momentum equation 1.3. Where u is flow velocity, ρ is gas density, and w' is instantaneous rate of production for the combustion gases.

$$\frac{d\rho}{dt} + \frac{d}{dx}(\bar{\rho}u' + \bar{u}\rho') = \frac{dw'}{dx} \quad (1.2)$$

$$\frac{d}{dt}(\bar{\rho}u' + \bar{u}\rho') + \frac{d}{dx}(2\bar{\rho}\bar{u}u' + \bar{u}^2\bar{\rho}') = -\frac{dP'}{dx} \quad (1.3)$$

Many of these investigations provide a linear analysis of the interaction of unsteady heat release rate and acoustic pressure but these only predict the frequency of the limit-cycle oscillations. Culick has presented a nonlinear dynamic model to predict the amplitude of oscillations after the onset of thermoacoustic instability within a combustion chamber. His work focused on an application towards modeling instabilities within rocket engines, ramjets, and thrust augmenters but concluded with a model that can be used for a multitude of different combustor applications [13].

Peracchio used Culick's acoustic model and developed their own heat release model to predict onset and amplitudes of limit-cycle oscillations within a scaled gas-turbine experiment [14]. Yang accompanies this with a third order nonlinear acoustic model and a second order nonlinear combustion model. He found that the acoustics affect the amplitude of the limit-cycle oscillations but the combustion response dictates how instabilities are triggered [15].

In 2002 Lieuwen noted that the thermoacoustic dynamics within a gas-turbine combustor simulator may be intrinsically stochastic [2]. Fichera observes that chaos is present within thermoacoustic dynamics when using a linear and nonlinear analysis approach [16]. In 2012 Kabiraj reported that even with a laminar flame, a type-two state of intermittency was present within pressure field dynamics [17].

Some theoretical investigations may use the acoustic model to determine linear stability limits of a specified system such as a gas-turbine [18]. Another paper introduces the linearized Euler equation method to model the high frequency longitudinal waves within a combustion chamber [19]. The acoustic wave models have also been used in conjunction with Computational Fluid Dynamics, CFD, to model the affects of combustion instability within a flow [20, 21]. These are limited however, to their relevant engineering applications.

More recently, the flame transfer function, FTF, and the flame describing function, FDF, have been used to create a general mathematical model of thermoacoustic instability. The FTF predicts the response of a flame to external perturbations within the frequency domain [22, 23], shown in equation 1.4. In this equation $F(\omega)$ is the FTF in the frequency domain. q is the heat release rate fluctuation and Q is the mean heat release rate. u is the velocity fluctuation and U is mean velocity within the chamber's flow field. ω is the angular frequency in radians [24].

Applications of FTF's include a gas-turbine combustor to examines how the flame structure is affected by the velocity perturbation input [25, 26, 27, 28]. Schuller developed a model [29] which investigated the response of a premixed, anchored flame to velocity perturbations, commenting that flames possess characteristics similar to low-pass filters [30].

$$F(\omega) = \frac{q(\omega)/Q}{u(\omega)/U} = G(\omega)e^{i\phi(\omega)} \quad (1.4)$$

The flame transfer function is a linearized approach to predicting the coupling between unsteady heat release rate and acoustic pressure and therefore will not capture the rich nonlinear dynamic details of thermoacoustics. For a more detailed approach, FDF's consider nonlinearities within the system and can predict amplitudes, frequency shifts, and other nonlinear traits. The FDF builds on the framework of FTF by introducing a sinusoidal forced perturbation which develops a nonlinear, harmonic response from the flame [31, 32, 33, 34]. Equation 1.5 shows the controls equation in the frequency domain of an FDF($F(\omega, |u|)$) where ω is the frequency and u is the amplitude from the forced sinusoidal perturbation.

$$F(\omega, |u|) = \frac{q(\omega)/Q}{u(\omega)/U} = G(\omega, |u|)e^{i\phi(\omega, |u|)} \quad (1.5)$$

Mathematical models to predict the onset of thermoacoustic instability such as the FTF and FDF rely on a forced pressure perturbation to analyze the response of the flame and may only capture the dynamics of linear and harmonic systems [35]. In general, combustion devices do not impose specified acoustic vibrations onto their enclosed flame and will instead develop thermoacoustic instabilities through synchronization[36].

The synchronization of pressure and heat release rate has been proven to cause thermoacoustic instability while lacking any forced perturbation. Depending on the dynamic states of the system, the heat release and pressure can be either synchronized or de-synchronized. A variety of studies by Mondal. found various synchronization states including phase locking, intermittent phase locking, and even phase drifting [37].

Within synchronization, the pressure and heat release rate may also be interpreted as two oscillators within a system [38]. The amount of flames and their relation to each other will therefore affect the observed dynamics during thermoacoustic instability. Manoj investigates multiple candle flame oscillators and notes that the dynamical state will depend on the number

of oscillators present in the system [39].

While previous and ongoing research provides great insight into the physical phenomena of thermoacoustic instability, fundamental experiments are required in order to further understand its underlying dynamics.

1.3 General Studies on the Rijke Tube

A Rijke tube is a combustion device consisting of a heat source and an air column with at least one open end [40]. The air column acts as the chamber with simply defined acoustic characteristics. The heat source, centered radially within the tube, can change its relative position along the length of the tube. This elegant system is able to develop self-excited thermoacoustic instability without the need for any external perturbations [41]. This was first noted by Professor Rijke in 1859 when he placed a heated iron wire gauze into a glass tube and observed that the resulting sound was approximately the same as the harmonic frequency of the tube [42]. A simplified diagram of a Rijke tube is shown in figure 1.3.

The Rijke tube is a strong tool to study the dynamics of thermoacoustic without requiring complex combustor setups [43]. The mechanisms of the Rijke tube are based on the in-compressible flow equations with small perturbations of velocity and pressure [44, 45]. This has been proven with previously conducted experiments in a Rijke tube using an electronic heater. The overall hydrodynamic flow within the tube are shown in equations 1.6 and 1.7. We assume no mean flow within the tube and define any perturbations as wave equations [46]. Where P' is the acoustic pressure perturbation and u' is the velocity perturbation within the flow field. P' and u' are both functions of location from the top of the tube(x) and time(t). L is the length of the Rijke tube.

$$P' = P_n \sin(nxL) \cos(t) \quad (1.6)$$

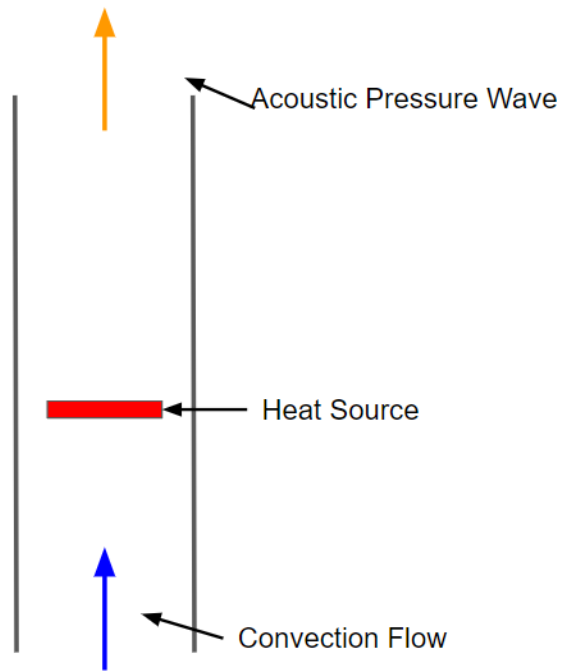


Figure 1.3. Diagram of a Rijke Tube

$$u' = -U_n \cos(nxL) \sin(t) \quad (1.7)$$

The harmonic frequencies of the tube, ω , are approximated with the air column length and the speed of sound. Equations 1.8 and 1.9 calculate the fundamental frequency of a standing wave in an air column with both ends open and one end closed. During thermoacoustic instability, the observed dominant frequencies will be based off of the fundamental frequencies of the tube.

$$\omega = \frac{n\pi c}{2L} \quad (1.8)$$

$$\omega = \frac{n\pi c}{4L} \quad (1.9)$$

Thermoacoustic combustion experiments have been conducted using Rijke tubes in the past few decades. Laminar, premixed flames are capable of fully developing self excited thermoacoustic

oscillations within these setups [47]. Noble investigates the thermoacoustic states of a rich methane-fueled flame [48]. Kabiraj proves that an unstable, quasi-periodic state was present within a lean flame fueled with natural gas [17]. In another publication, Kabiraj focuses on the quasi-periodic state during thermoacoustic instability of a laminar, premixed flame where the flame eventually blows out [49]. The hydrodynamic region was also investigated within the Rijke tube with a laminar, premixed flame [50]. Guan notes strange nonchaotic attractors are present before chaos occurs with a laminar flame within a Rijke tube [51].

The diverse set of dynamics observed in multiple experiments utilizing a Rijke tube proves its effectiveness to study the fundamentals of thermoacoustic instability. In this paper, we will construct an experimental setup with a Rijke tube to study combustion instability with a variety of laminar, premixed flames.

1.4 The goal of the present study

The goal of the present study is to develop a Rijke tube setup and to investigate the effect of flame interaction on the pressure and intensity dynamics during thermoacoustic instability. Previous work studying on this topic have observed different dynamical states of the pressure and the heat release rate. Traditionally, many investigations will consider the flame as a singular heater element. However, these investigations will utilize multi-flame burners that may affect the dynamical states of pressure and heat release rate when compared to a single, conical flame.

Kabiraj reports many dynamic states in the acoustic pressure field, including chaos [52]. Kasthuri uses a matrix burner with 112 injectors to study the route to thermoacoustic instability in a multiple flame burner, reporting bursting and mixed-mode dynamics [53]. Culler investigates the affect asymmetrical and unsymmetrical equivalence ratios in a multi-flame combustor, noting that the nozzle configuration greatly influences the bifurcation as well as fuel staging for a gas turbine engine [54].

It is important to note that these multi-flame burners are not similar to meshes or plugs

that anchor the flame. Porous media plugs provide more surface area for heat re-circulation to the cold, premixed gas during combustion [55] [56] [57]. It can be observed however that these tips are small enough to maintain a single conical flame on the burner as used by Guan [51] and Zhao [50]. The wire mesh is much more fine than the orifices of multi-flame tips and therefore cannot easily produce individual flames during operation.

Due to the observation that multi-flame burners greatly influences the dynamics in thermoacoustic instability, we introduce a systematic experimental investigation into the thermoacoustic phenomena of three different multi-flame burners as well as a single-flame burner. By changing the burner from a single flame to multiple flames, we note major changes in the dynamical states of pressure and heat release rate of a laminar, premixed flame within a Rijke tube.

1.5 Outline of the thesis

The thesis is divided into 4 main chapters. Chapter 1, previous to this outline, provides background information and general studies on both thermoacoustics and the Rijke tube. The fifth section introduces the goal of the present study.

Chapter 2, section 1 reviews how the Rijke tube was configured and why a high speed camera and pressure sensors were selected for data collection. It also explains why a laminar, premixed flame was used. Section 2 reviews the newly designed experimental setup used for pressure and heat release rate data collection during the systematic investigation of local flame interactions effect on thermoacoustics. This reviews how the high speed camera was used and what data was collected for each of the four experiments.

Chapter 3 explains the results obtained from the initial setup. This includes the supporting results for Rijke tube diameter sizing. The final setup is also reviewed here, including an overview of the pressure and heat release rate measurement methods.

Chapter 4 systematically investigates the effect of multi-flame burners on the pressure

field during thermoacoustic instability. This is divided into the following subsections, a comparison of the single flame and seven flame experiments, the in-line three flame experiment P' dynamics, a study of the synchronization of each heat release rate and P' , and a comparison of the in-line three flame experiment to the asymmetrical three flame case.

The conclusion in presents the overall findings and their impact on the topic of thermoacoustics. It also provides potential avenues for future studies within this area of research.

Chapter 2

Methodology

2.1 Rijke Tube Experimental Setup Development

2.1.1 Selection of Rijke Tube Parameters

An initial setup was developed in order to test key parameters of the Rijke tube system. These include diameter of the tube, heat release rate acquisition, and temperature of the location of the pressure sensor. Figure 2.1 shows the diagram of the experimental setup.

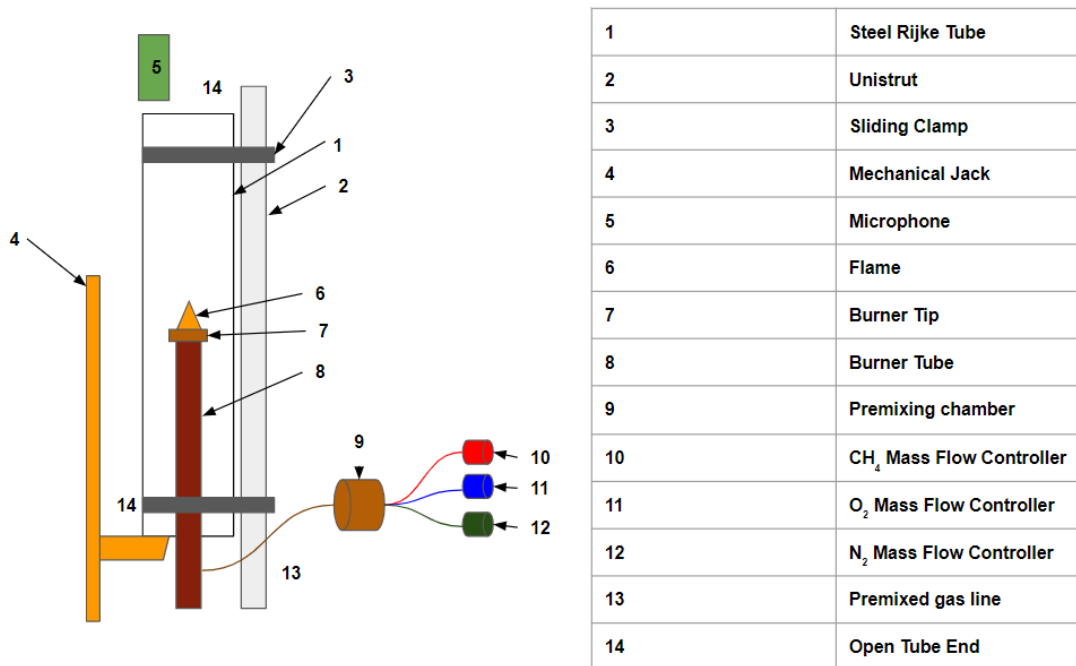


Figure 2.1. General Rijke Tube Setup Diagram.

This experimental apparatus consisted of a conical flame burner and multiple steel tubes. A 1.33 meter long copper tube with an inner diameter of 12.7mm and an outer diameter of 16mm is used for the burner tube. The burner tube is connected to a premixing chamber further upstream, where methane, oxygen, and nitrogen are mixed based on preset flow rate conditions. The mass flow for methane, oxygen, and nitrogen are set using an Alicat digital flow controller for each gas.

The copper burner tube allows for multiple brass inserts to gently press fit into the top of the tube. This allows the use of different flame configurations during experiments. Different open-ended diameter steel tubes were tested for sizing the Rijke tube. The different diameters were 72.9 mm, 50.8 mm and 25.4 mm. The length was held constant at 914mm.

Plastic aligners were placed within the steel tubes to ensure the burner was centered radially within the Rijke tube. The vertical motion of the tube was controlled with a mechanical jack and the tube was constrained to a vertical steel channel so that it only moved in the z-direction.

Multiple experiments with a premixed, laminar flame were conducted to ensure the onset of thermoacoustic instability was obtained. Sound measurements were recorded with a microphone held by hand approximately 25 mm above the Rijke tube. Examples of test data may be found in the appendix.

Temperature measurements also were conducted with an Omega K-type thermocouple and read with an Omega DP460 digital panel meter in order to ensure the acoustic pressure sensor port on the top of the tube does not experience temperatures above 120 degrees Celsius per PCB's technical specifications. The setup diagram can be viewed in the appendix.

2.1.2 Flame Configuration

There are four well known mechanisms to cause the onset of combustion instability. These include changes in the local equivalence ratio, coherent flow structures, entropy waves, and flame surface area modulation [1]. For a premixed flame utilizing gaseous fuel and oxidizers,

the equivalence ratio cannot oscillate with the acoustic pressure field because it is already constant once it reaches the flame front. Premixed flames do not require vaporization of liquid fuels, mitigating the risk of feedback between the acoustic pressure and fuel and oxidizer mixing process.

A laminar system does not possess any relative high speed flow within the chamber. This mitigates the risk of synchronization of vortex shedding affecting the acoustic pressure during the combustion process. The conical shape of a laminar flame allows for easy heat release rate measurements by recording the intensity of the flame. Due to the asymmetrical geometry of the flame, a two-dimensional image may accurately record the intensity. A laminar flame may also possess less flow noise and more stable operation, minimizing potential background noise in pressure and heat release rate data collection.

The two dominant ways that the premixed laminar flame may develop thermoacoustic instability is therefore entropy waves and flame surface area modulation. The entropy waves occur within the Rijke tube chamber as the heat from the flame creates a sharp temperature gradient along the tube. This is therefore the key factor in the onset of self-excited thermoacoustics within a Rijke tube. Once the pressure is unstable, the acoustic disturbances transfer along the flame front of the laminar, conical flames. The effective surface area of the flames changes, which is directly proportional to the heat release. The flame is then responding to the entropy waves and develops the positive feedback cycle that will sustain the instability until an outside factor influences the system.

Methane is utilized as the main source of fuel for many combustion applications stemming from gas-turbines, internal combustion engines, and rockets. Methane is gaseous at room temperature and is the lightest of the hydrocarbons. It also produces the least soot compared to other fuels while emitting bright CH^* molecules during combustion. The CH^* molecules are chemiluminescent, emitting light at approximately 425nm, which is brightest at the flame front. These attributes ensure high speed imaging is consistently clear during all experiments.

2.2 Multi-flame Dynamics Experimental Setup

The final Rijke tube experimental setup is shown in figure 2.2 which consists of a burner mounted co-axially within a vertical fused quartz-glass tube. A 1.33 meter long copper tube with an inner diameter of 12.7 mm and an outer diameter of 16 mm is used for the burner tube. Multiple brass inserts are designed to fit into the top of the copper burner tube. Two meshes are

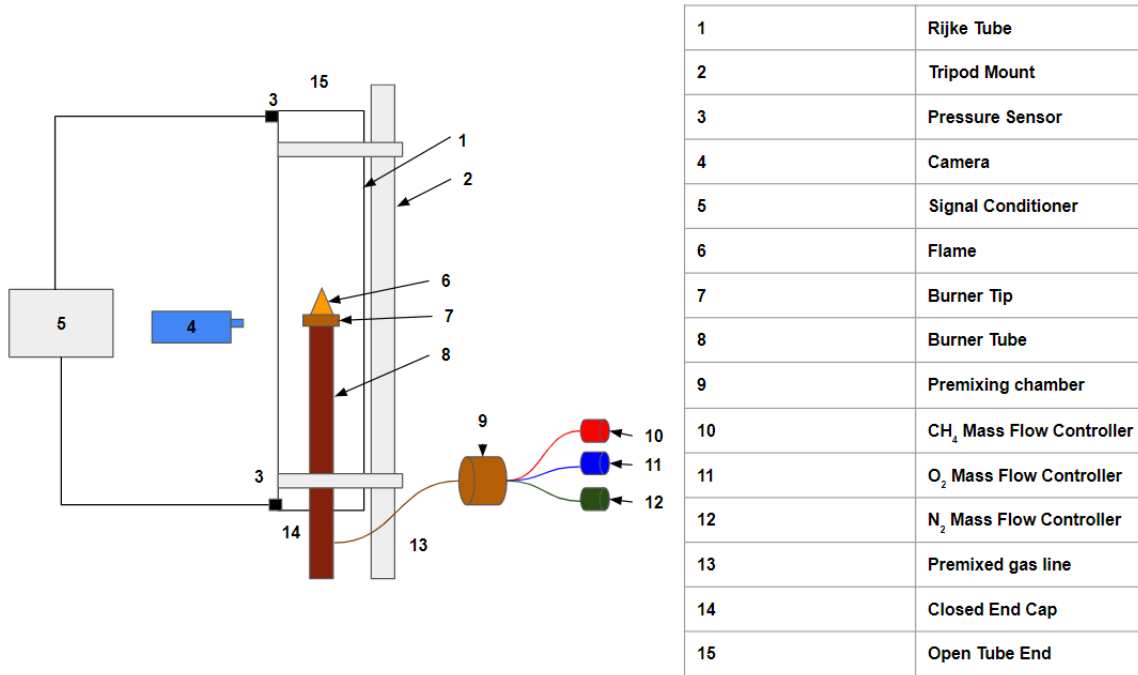


Figure 2.2. Final Experimental Rijke tube setup model.

placed at the bottom of the copper tube to prevent further flashback as well as aid in maintaining a laminar flow of ambient pressure gas through the burner tube. The burner tube is mounted to a vertical steel strut with 2 clamps and is held in place with a spring clamp. A high temperature Teflon plastic aligner ring is mounted approximately 152mm below the burner tip to prevent radial movement of the burner tube within the Rijke tube.

The burner tube is connected to a premixing chamber further upstream, where methane, oxygen, and nitrogen are mixed based on preset flow rate conditions. The mass flow for methane, oxygen, and nitrogen are set using an Alicat digital flow meter for each gas. Oxygen and

nitrogen are used instead of air in order to more accurately control the flame temperature during experiments.

The Rijke tube consists of a 914mm long, clear quartz-glass tube with an inner diameter of 50mm and a wall thickness of 2.5mm. The quartz tube is mounted onto an aluminum rail by two aluminum clamps on the top and bottom of the tube. A machined brass cap is mounted on top of the quartz tube and aluminum clamp. The cap has a PCB model 103B02 acoustic pressure sensor connected with a brass tee fitting. There is a quarter wavelength closed-end tube attached to the pressure sensor port on the brass cap in order to filter out noise above 800 Hz. A Moog Hercules tripod is used to translate the quartz tube vertically with respect to the burner tip, thereby changing the relative flame location within the tube. The bottom of the Rijke tube is closed with an ABS plastic cap. The bottom cap also has a radially centered hole for the burner tube to fit through. This provides a natural frequency of 93Hz when the air in the column is at room temperature. The cap includes a pressure sensor port that mounts a PCB 103B02 sensor by gently press-fitting the sensor into a tube that has a 3mm orifice feeding directly into the chamber. Both pressure sensors are powered with and send data through a PCB 482A16 signal conditioner. Flame location is read with a scale mounted onto the aluminum rail.

The pressure sensors were tested with a signal generator and speaker. They each read a 750Hz signal as setup in figure 4.4 in the appendix. The sensors were tested at the same time and were fixed on the test setup at one end of the open aluminium tube. The speaker was fixed to the other end of the tube and generated an acoustic standing wave at a specified frequency. The sensors read exactly 750Hz. The amplitudes may be shifted by approximately 8Pa but the range of amplitudes read are the same. Refer to figures 4.5 and 4.6 in the appendix for the time series and PSD of the 750Hz signal test. The background noise of the experimental setup in the lab was also read by the pressure sensor in the bottom of the tube, as that was the selected location due to the close proximity to a pressure anti node. The background noise is maximum 5Pa, which is negligible compared to the sound produced during thermoacoustic instability. Refer to figure 4.3 in the appendix for the background measurement. The pressure sensors are therefore verified to

read accurate signals and are usable for measuring P' during thermoacoustics experiments.

A Phantom V710 high speed camera is used to capture images of the flames during experiments. The images are captured at 2000 frames per second with an exposure time of 490 microseconds. Three seconds of data are recorded by the high speed camera. By utilizing a 425NM X 25NM filter, the background noise is mitigated and the flame front is the brightest object in each image frame. The two dimensional image of the conical flame provides the diameter of the shape along the entire flame, which is linearly proportional to the surface area of the conical shape. Brightness may be summed across the entire frame, producing an instantaneous value that is therefore linearly proportional to heat release rate [58], [59], [37]. Due to the linear proportionality of flame surface area to heat release rate of a conical flame, high speed images of the flame front may therefore be an accurate diagnostic method to obtain heat release rate modulation. Figure 2.3 compares the stable shape of a conical flame to an instantaneous frame during thermoacoustic instability. The change in the two dimensional shape may correlate directly to the surface area modulation because of the asymmetrical geometry of the flame. This is also a clear, visual indication of heat release rate fluctuation from the flame to the flow field.

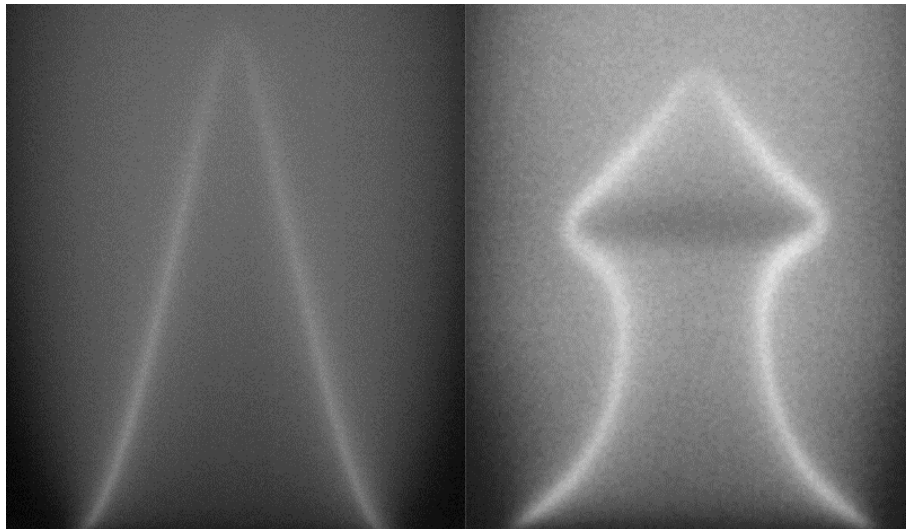


Figure 2.3. Comparison of a conical flame during stable operation (left) and during thermoacoustic instability(right)

Four different burner configurations were tested within the Rijke tube; a single flame, seven flame, triangular three flame, and an in-line three flame tip which are shown in figure 2.4. They were gently press fit into the top of the burner tube during their respective experiments. The equivalence ratio was held constant for all experiments at 0.85. Oxygen in the Oxygen-Nitrogen mixture was 25 percent for the single and three flame experiments.





Burner	Diagram	Hole Count	Hole Diameter (mm)	Total Area(mm ²)	Flow Rate (SLPM)	Mean Velocity (cm/s)
1H		1	11.176	71.33	10	169.9
7H		7	3.80	79.4	8	167.9
3HL		3	4.09	39.4	4	169.2
3HT		3	4.09	39.4	4	169.2

Figure 2.4. Four burner tips and their respective diagrams

The flame speed was 47.1cm/s and the flame temperature was 2258.7K . The seven flame experiment had a 23 percent oxygen percentage level as the flame blew off very quickly before reaching the bottom half of the Rijke tube if the oxygen percentage was any higher. For this the flame speed was 42.6cm/s and the flame temperature was 2169.5K . The gas velocity of the Methane, Oxygen, and Nitrogen mixture was held constant for each experiment. This was approximately 38.0cm/s at the entrance of the every orifice for all burner tips. Due to the different cross sectional areas, the mass flow rate was modified to ensure the constant velocity. The single flame experiment had a total volumetric flow rate of 10 SLPM as the tip has the largest overall area. The seven flame experiment was conducted at 8 SLPM and the three flame experiment had a flow rate of 4 SLPM. The flame distances are approximately the same for both of the three-flame tips. The laminar flame speed and temperature were calculated using ANSYS Chemkin [60].

Chapter 3

Results

3.1 Characterization of a Rijke Tube Based on Dynamics of a Single-Flame

The 72.9mm diameter tube did not produce any unstable response of a laminar, conical flame. The 25.4mm diameter tube produced audible thermoacoustics but there were visible burn marks on the outer wall of the steel. This may have been a result of the flame's distance to the wall, overheating the tube. The 50.8mm diameter tube produced audible thermoacoustic instability and that diameter was therefore selected for the final setup. Refer to figure 4.1 and 4.2 in the appendix for the time series P' recorded in the steel tube. The fundamental frequency was read, strongly supporting that synchronization occurred between the flame and pressure field within the selected tube.

The temperature of the pressure sensor fitting was measured to ensure it is within working limits as specified by PCB. A hole was drilled into the top of the 50.8 mm tube and a tee fitting was fabricated from standard brass fittings. The flame used for these tests had an equivalence ratio of 0.9 and a mixture of 32 percent Oxygen and 68 percent nitrogen was used. The flame temperature was approximately 2518 Kelvin, which is higher than the flame temperature used for the final results. The temperature of the pressure sensor fitting did not exceed 120 degrees Celsius after 45 minutes of testing.

The high speed camera may only accurately record flame intensity at 2000 fps with a 490

microsecond exposure time if the CH filter is attached. The intensity value is found by summing the brightness values within the images. By using the CH filter, the only light to pass into the camera's sensor is from the conical flame edges.

The high speed camera was selected for experimental data collection because of its ability to recognize separate flames within the Rijke tube.

3.2 A Systematic Investigation of The Affect of Multi-Flame Dynamics on Thermoacoustic Instability

3.2.1 Single Flame and Seven Flame Experiments

When using the single flame burner tip, no noticeable change in the acoustic pressure over the entire length of the tube was observed. As seen in Fig. 3.1, the pressure bifurcation plot only shows flow noise at each step [61]. The single flame therefore maintains steady state combustion through the length of the Rijke tube. However, when using a seven flame burner tip, the dynamical response becomes much more complex and the amplitude ranges up to 200Pa. There are multiple bifurcations points that can be observed in figure 3.1. This strongly supports the existence of a variety of dynamical states throughout the length of the tube.

The 1H experiment image set is shown in figure 3.2. From the 8 frames there is a lack of noticeable change in the flame's surface area. This supports the P' data where no thermoacoustic instability occurred. The single flame did not synchronize with the pressure within the Rijke tube. The 7H image set provides a much different picture than the 1H case, as can be observed in figure 3.3. All seven flames are oscillating, extinguishing, and reigniting in seemingly different frames. An overall oscillation also seems to exist where the left flames extinguish and reignite and then the right side performs the same pattern. This visually confirms that \dot{q}' is strongly interacting with P' due to the major changes in flame surface area as well as the extinguish and re-ignition of the individual flames. The only major change between the single-flame and seven-flame experiments was the addition of multiple flames on the burner tip. It is therefore

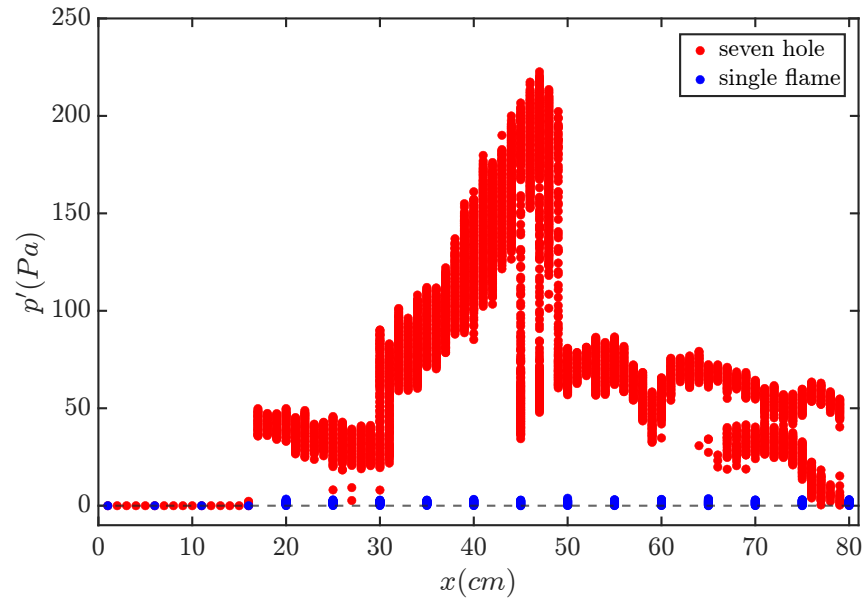


Figure 3.1. P' bifurcation plots for the seven-flame and single-flame experiments. The seven-flame P' data was taken in 1cm intervals and the single-flame data was taken in 5cm intervals.

necessary to investigate how the different flames on the burner tip affect the pressure dynamics.

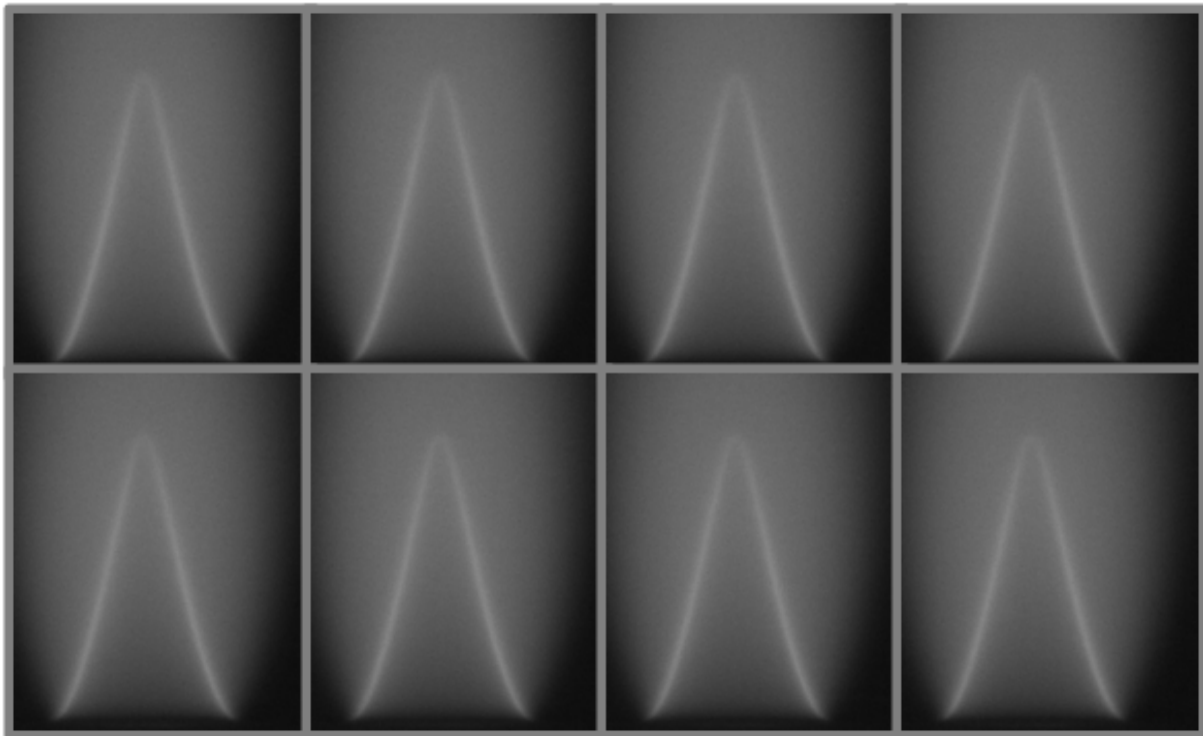


Figure 3.2. Unfiltered image set of the single flame at 20cm.

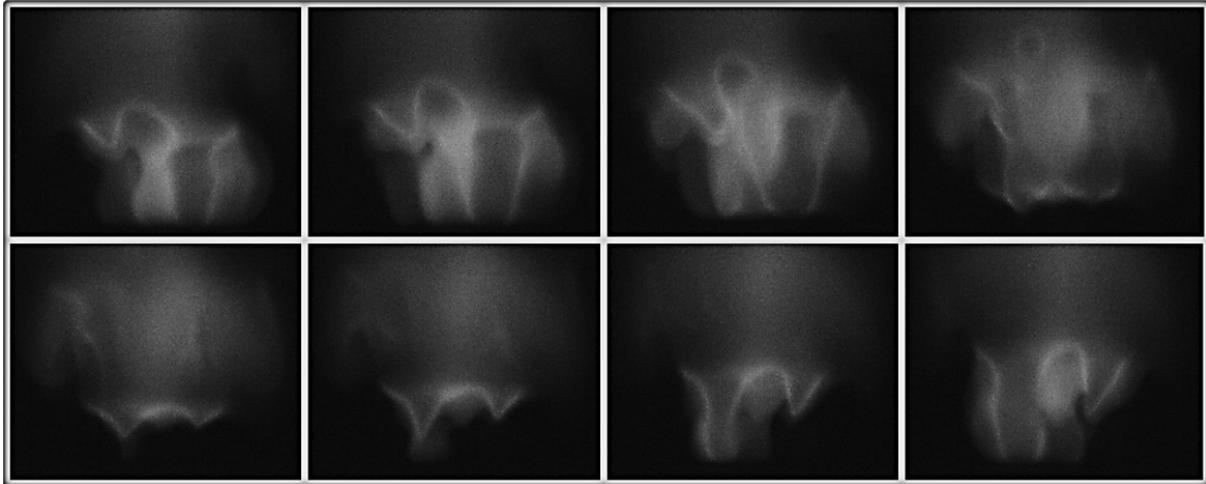


Figure 3.3. Unfiltered images of the 7H burner tip at 39cm.

3.2.2 Linear Three Flame Experiment

The 3HL burner tip is unique in that it enables heat release rate data to be collected on each flame from high speed camera image sets. These can then be quantitatively analyzed to observe how each flame influences the P' time series observed within the Rijke tube.

The Pressure bifurcation plot of the three-flame experiment shows multiple bifurcation points along the length of the Rijke tube. This is observed in figure 3.4 with many clear changes in the amplitude range of P' as x increases. Even with the exact same flame conditions, the 3HL P' bifurcation plot represents a variety of dynamical states whereas the 1H experiment maintained steady-state.

Due to the variety of amplitude ranges in P' observed in figure 3.4, individual time series must be investigated to further understand the underlying dynamics. There are five representative locations at 22cm, 33cm, 46cm, 59cm, and 70cm.

Figure 3.5 shows P' over 10 seconds as well as the power spectral density(PSD) and reconstructed phase space for the five locations along the length of the Rijke tube. The 5 rows of subplots represent four unique, different observed dynamical states from the bifurcation in figure 3.4. The first half of the tube has a dominant frequency of around 300Hz and the lower half is approximately 185Hz as seen in the PSD graphs.

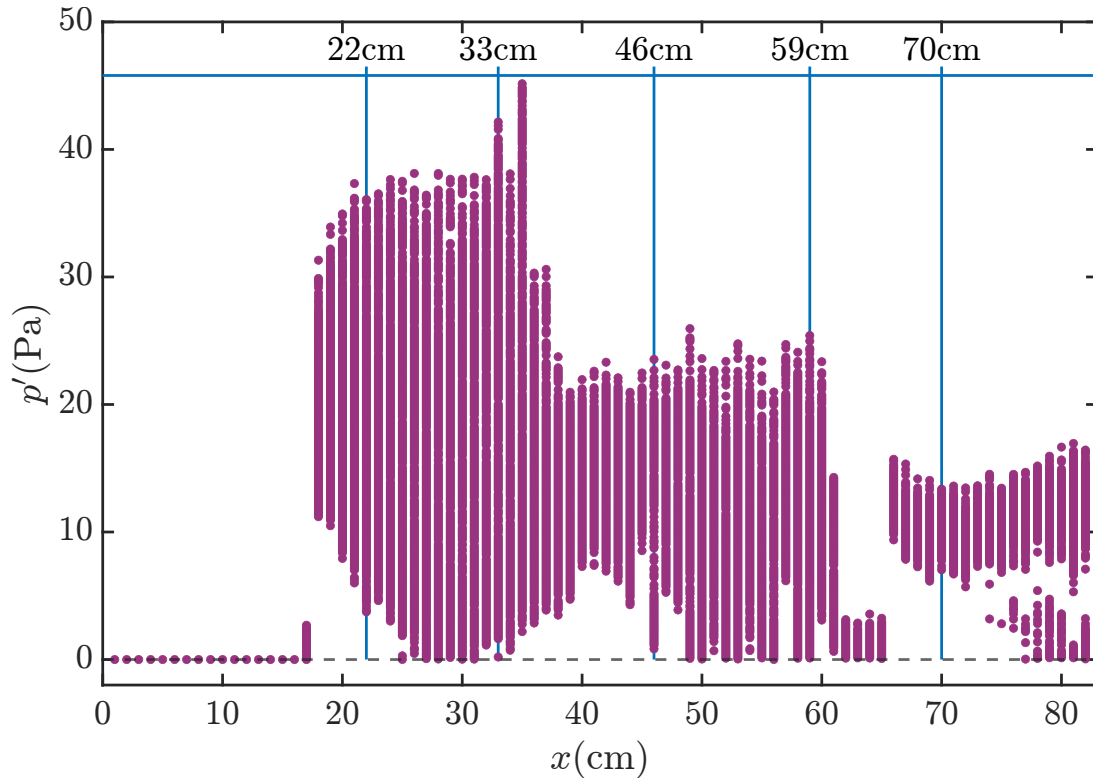


Figure 3.4. In-line three flame P' bifurcation plot from 0cm to 82cm in 1cm intervals.

The 22cm location, figure 3.5 shows two peaks above and below 302.2Hz by 6.7Hz. The lower frequency matches the cyclic pattern of high amplitude peaks observed within the time series data. The phase space shows two dominant rings which is representative of the on-off pattern from fish-bone instability.

The lower order frequency is present through the initial mixed-mode section seen in 33cm. However, due to the presence of small periodic sections, the 6.7Hz higher and lower peaks are not as easily identifiable within the PSD of P' . The dominant frequency mode is similar to fish-bone instability at 293Hz. The phase space does not possess as easily recognizable rings as observed in fish-bone instability.

Further into mixed-mode, at 46cm, the frequency peak at 287Hz broadens and specific values are less noticeable in the PSD. There is also a lack of obvious low frequency peaks within the PSD of P' in figure 3.5. There are surrounding peaks that may be identified at 295.2Hz and 273.8Hz. The difference in frequencies between these modes is 13.2Hz. It can be seen that

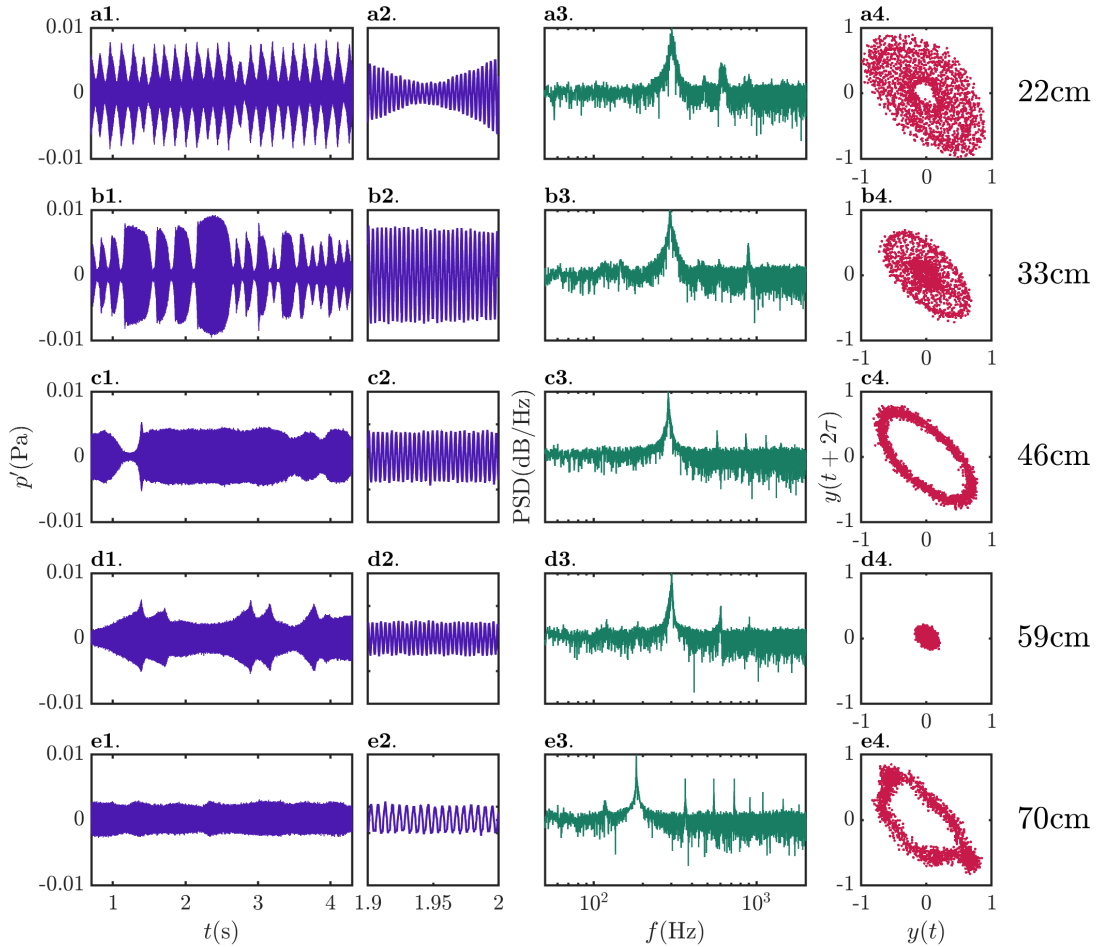


Figure 3.5. The time series(left 2 graphs), PSD(center right), and reconstructed phase space(right) of P' select locations along the Rijke tube.

there is a small peak at 14.8Hz which could account for the frequencies surrounding the 287Hz dominant peak. The phase space of this location possesses an obvious outer ring which may be from the long bursts of periodic instability.

During burst mode at 59cm, the dominant frequency peak at 300.6Hz broadens and there are some lower frequency peaks at 5.7Hz as well but they do not seem related to the overall high amplitude modulation pattern within the P' time series. Figure 3.5 shows the bursting pattern. The time series follows a 300Hz dominant frequency but lacks any notion of a lower frequency such as what is observed in fish-bone instability. There are no obvious peaks within the broadband surrounding 300.6Hz. The phase space for the whole time series is a filled disk as

P' becomes steady and the amplitude ranges from 0Pa to 25Pa.

Clear, dominant peaks in the P' PSD are not present until the limit cycle oscillation state around 70cm as seen in figure 3.5. The dominant mode lowers to 182.5Hz and there is a small peak at 116.9 Hz and 60Hz but there is a lack of broadband frequency ranges as previously seen in the other instability modes. The phase space follows a much more obvious pattern, maintaining a fairly constant peak relative to the other locations. However, the shape is not perfectly round which may be from the slight amplitude modulation seen in the time series.

The reconstructed phase space utilizes 6 dimensions and the subplots in figure 3.5 shows the first 3. The false nearest neighbor (FNN) method was used to calculate the minimum dimension required for the phase space reconstruction [62]. This ensures the prevention of false crossings of trajectories within the space. The FNN graphed for up to 6 dimensions is shown in the appendix for each P' time series location.

$$P'(n) = [P'(n), P'(n + \tau), P'(n + 2\tau), \dots, P'(n + 5\tau)] \quad (3.1)$$

No P' time series required above 5 dimensions based on the false nearest neighbor method. Therefore a dimension of 6 was used in forming the reconstructed phase spaces in figure 3.5. The time lag, τ , for the reconstructed phase space was calculated by finding the minimum correlation value from the time series. The auto-correlation, r_k is found in equation 3.2 through 3.3.

$$r_k = \frac{c_k}{c_0} \quad (3.2)$$

$$c_k = \frac{1}{T} \sum_{t=1}^{T-k} (y_t - \bar{y})(y_{t+k} - \bar{y}) \quad (3.3)$$

c_0 is the sample variance of the time series and T is the effective sample size of the P' time series. Once the r_k value closest to zero was found, the corresponding lag was used as τ for

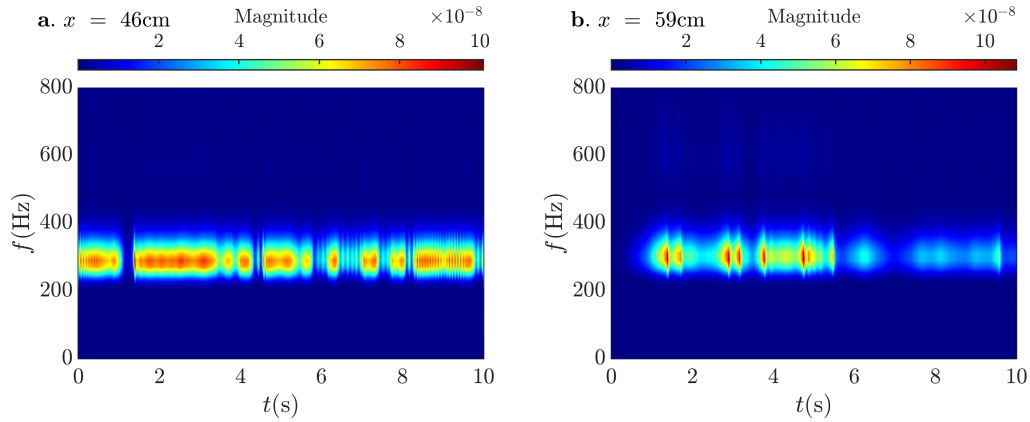


Figure 3.6. Continuous wavelet transform for P' of 46cm, mixed mode(left), and 59cm, burst mode(right).

reconstructing the phase space.

Due to the transient nature of mixed mode and burst mode instability, the continuous wavelet transform(*CWT*) is required to further understand the dynamics of the P' time series for mixed-mode and bursting. Figure 3.6 shows the *CWT* of 46cm, mixed mode(left), and 59cm, burst mode(right) for ten seconds of P' data.

The *CWT* in figure 3.6 shows that the dominant frequency is not present in between the large amplitude regions during mixed mode and burst mode instability. When instability is occurring, the *CWT* shows an approximate 100Hz range around the instantaneous dominant frequency. The lower frequencies observed in figure 3.5 are not present in the *CWT*'s and therefore could stem from the long-term patterns observed in each state.

3.2.3 Synchronization Analysis

Due to the variety in observed dynamics of P', the effect of heat release rate on the P' dynamics and their degree of synchronization must be investigated. The phase-lock-value(*PLV*) and root mean frequency(*RMF*) are therefore taken for each location along the Rijke tube for P'

and \dot{q}' . θ is the unwrapped instantaneous phase of each time series.

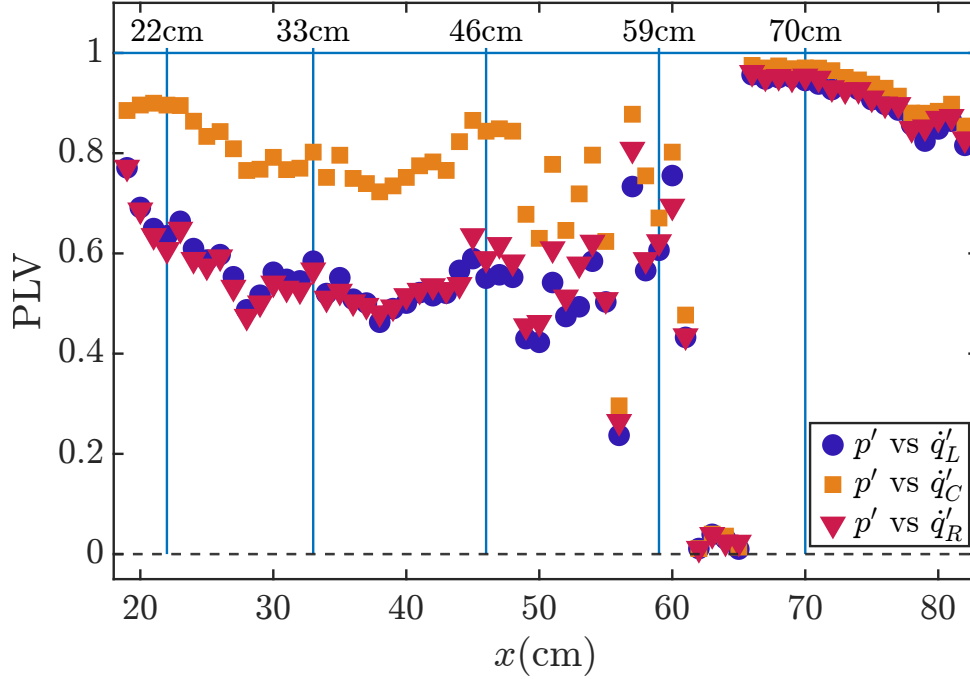


Figure 3.7. Phase Lock Value of P' and all three \dot{q}' for each location past the initial bifurcation point.

Equation 3.4 shows how PLV was calculated between P' and \dot{q}' .

$$PLV = N^{-1} \left| \sum_{t=1}^N \exp(i\Delta\theta_t) \right| \quad (3.4)$$

The PLV is near 1 for perfectly synchronized states and zero for perfectly un-synchronized oscillators. In figure 3.7 it is observed that P' is most in phase with the center flame and that the left and right are not synchronized with pressure until the limit cycle oscillations are reached in the bottom half of the Rijke tube. This may infer that \dot{q}'_C is influencing the P' dynamics to a stronger degree than \dot{q}'_L and \dot{q}'_R .

During fish-bone instability at 22cm, the PLV begins to decrease from approximately 0.9 to around 0.75 for the \dot{q}'_C and P'. \dot{q}'_L and \dot{q}'_R follow the same trend but possess lower overall PLV values than \dot{q}'_C when compared to P'. During mixed-mode oscillations preceding fish-bone instability around 33cm, the PLV stays constant until 36cm where it increases slightly.

After 43cm, the *PLV* between \dot{q}' and P' transition from a consistent value to a more random pattern. This could be due to how the P' dynamics possess sections of fish-bone, steady, and periodic instability where each \dot{q}' and P' may not necessarily be in phase.

Once the flame reaches 55cm, burst mode begins and the *PLV* observes a random spread of values through 62cm. The *PLV* ranges from 0.9 to nearly 0.3 as the flame moves down the Rijke tube. Past 62cm the pressure becomes steady and the *PLV* only compares sensor noise.

Limit cycle oscillations starting at 66cm past the steady location posses *PLV* values closest to 1 for all \dot{q}' 's and P' , indicating that the flames oscillate in-phase with each other and the heat release rate acts as a single entity influencing the pressure dynamics. There is however a decline to around 0.9 indicating that the pressure state may become quasi-periodic again.

$$\Delta\omega = |\omega_1 - \omega_2| \quad (3.5)$$

The relative mean frequency is shown in figure 3.8 which compares \dot{q}' and P' for each location in the Rijke tube. As seen in equation 3.5, the *RMF* of two time series is the difference in their mean frequencies where the mean frequency is an average of the first order time derivative of the instantaneous phase of the signal [37], [63].

The $\Delta\omega$ for \dot{q}'_C and P' is relatively low compared to \dot{q}'_L and \dot{q}'_R . This maintains the same value until mixed-mode where the *RMF* for \dot{q}'_L and P' steadily increase. Burst mode shows various random increases in $\Delta\omega$ until steady-state. $\Delta\omega$ drops and stays fairly constant for all \dot{q}' 's until 77cm where $\Delta\omega$ slowly starts to increase. The *RMF* supports the same trend that the *PLV* possesses in that \dot{q}'_C is much more synchronized with P' . We may conclude from these results that \dot{q}'_C could be driving the dynamics at a higher degree than the \dot{q}'_L and \dot{q}'_R . Figure 3.8 does provide a more clear picture as to how the degree of synchronization between \dot{q}' and P' changes when transitioning through dynamical states as x changes.

The *PLV* is also calculated for each \dot{q}' . Figure 3.9 shows the *PLV* between each flame across the length of the tube. It is observed that \dot{q}'_L and \dot{q}'_R generally have the highest *PLV* value

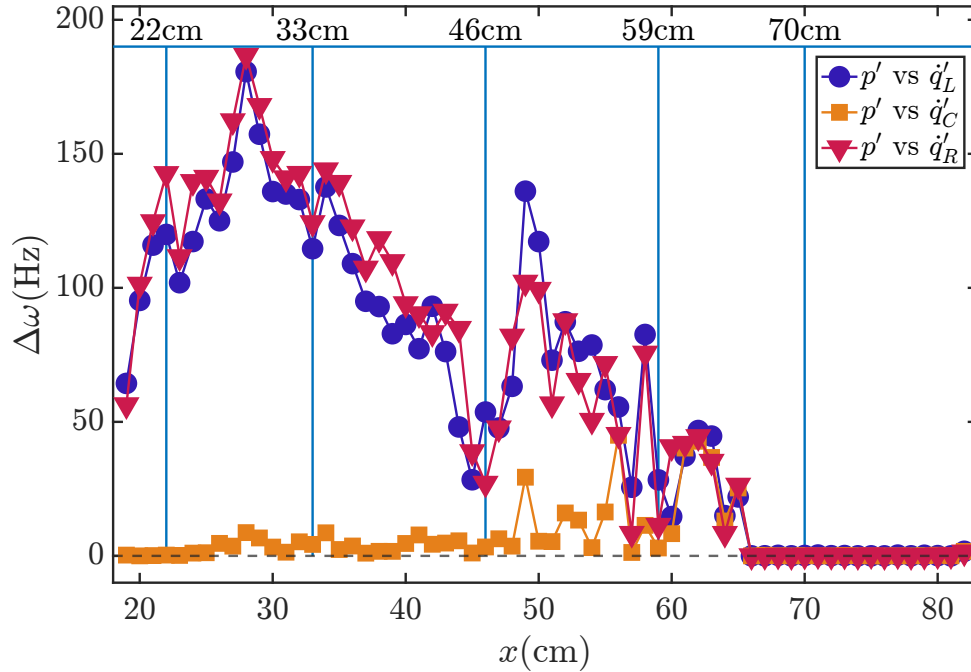


Figure 3.8. Relative mean frequency between \dot{q}' of each flame and P' for each location.

until burst mode. During burst mode the PLV for each case is lower but \dot{q}'_C is more synchronized with \dot{q}'_L and \dot{q}'_R as the burner tip moves down the tube. The PLV values do not all increase until the steady and periodic locations. For all other observed dynamical states, the PLV for \dot{q}'_L vs \dot{q}'_R are generally the highest.

The synchronization analysis in figures 3.7 and 3.8 compared P' and \dot{q}' time series corresponding to each location in the PLV plot. Figure 3.7 and figure 3.9 share similar overall patterns in x where the \dot{q}' 's were mostly out of phase during mixed and burst mode instability. It can be generally observed that \dot{q}'_L and \dot{q}'_R were in phase for most of the locations until bursting, where the PLV values for all \dot{q}' 's become very similar. It would be expected that \dot{q}'_L and \dot{q}'_R would be in phase much more compared to \dot{q}'_C , however there exists some variation in PLV values for \dot{q}'_L vs \dot{q}'_C and \dot{q}'_R vs \dot{q}'_C . The PLV does follow the overall expected trend that the outer flames are synchronized between each other compared to the center flame.

The PLV and RMF plots show that each \dot{q}' is synchronized with P' at different locations of x . It is therefore important to investigate how each \dot{q}' influences P' for two representative

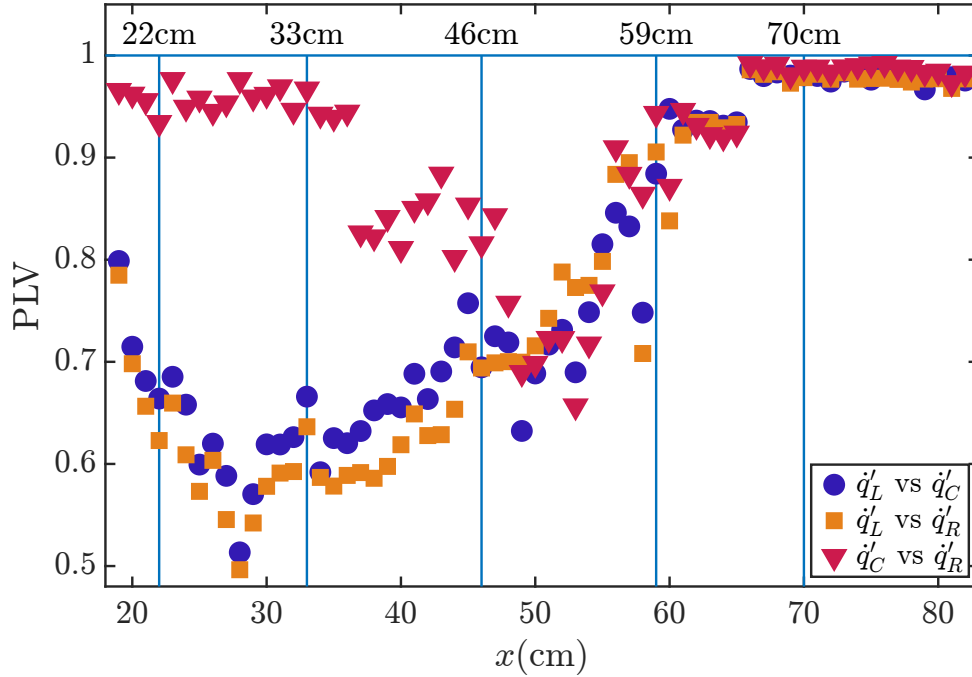


Figure 3.9. *PLV* between \dot{q}'_L , \dot{q}'_R , and \dot{q}'_C .

locations along the length of the Rijke tube. One location shall possess different degrees of synchronization between each \dot{q}' and P' and the other shall possess highly synchronized \dot{q}' and P' .

3.2.4 Dynamics of the Heat Release Rate

By using the phantom V710 high speed camera with a filter, we are able to capture the intensity of each flame individually. The images were divided into three section to separate \dot{q}'_L , \dot{q}'_C , and \dot{q}'_R as seen in the diagram of figure 3.10. Because the intensity is linearly proportional to the area modulation of a conical flame, the brightness of each flame can be summed within the images and used as instantaneous intensity modulation data for the heat release rate. The PSD of each \dot{q}' was calculated for 3 seconds of data for two representative cases: fish-bone instability and periodic instability.

We choose 22cm as a representative location due to a consistent fish-bone pattern within the P' time series across the entire data set. This provides much more clear example to investigate

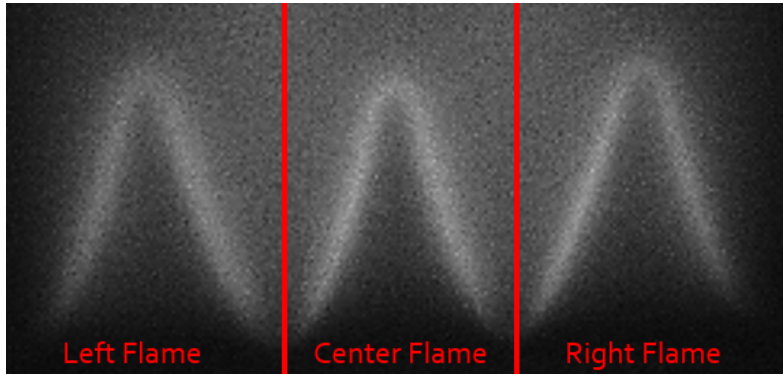


Figure 3.10. Image of the 3HL flames and how they are separated within the frame

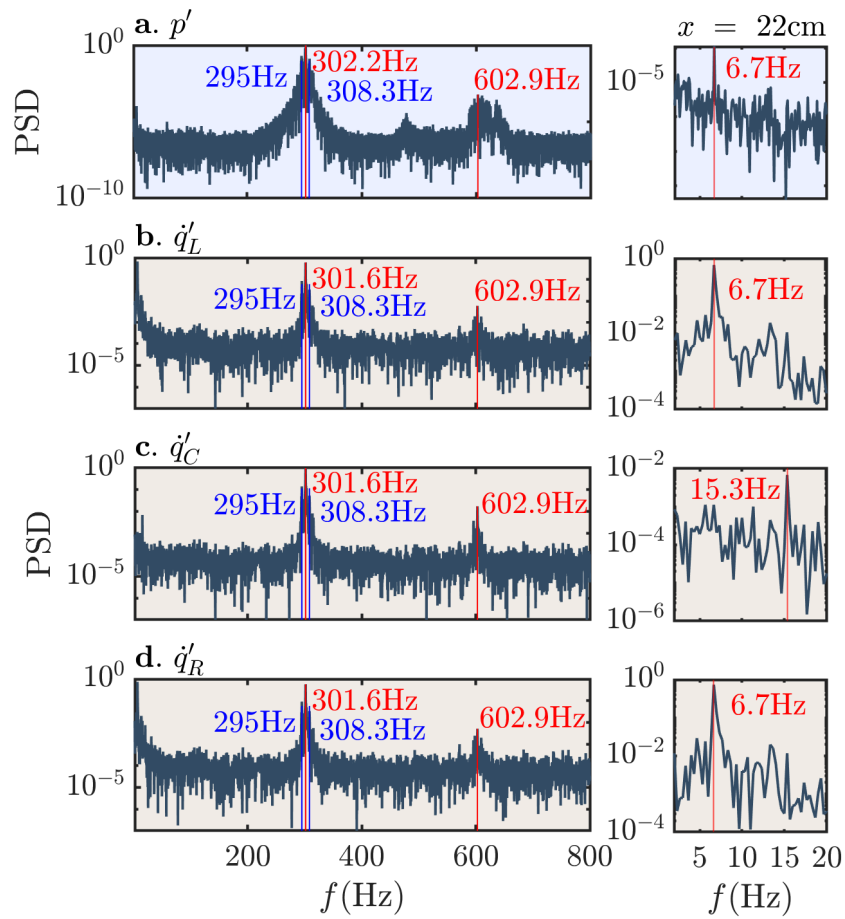


Figure 3.11. PSD's of each q' and P' at $x = 22\text{cm}$

the dynamics of the q' and P' data when compared to other more complex locations. In figure 3.11 we can observe that all q' 's exhibit a 301.6Hz dominant frequency, a low frequency of 6.7Hz may be observed in q'_R and q'_L . This low frequency is also present in the PSD of P' in figure 3.11.

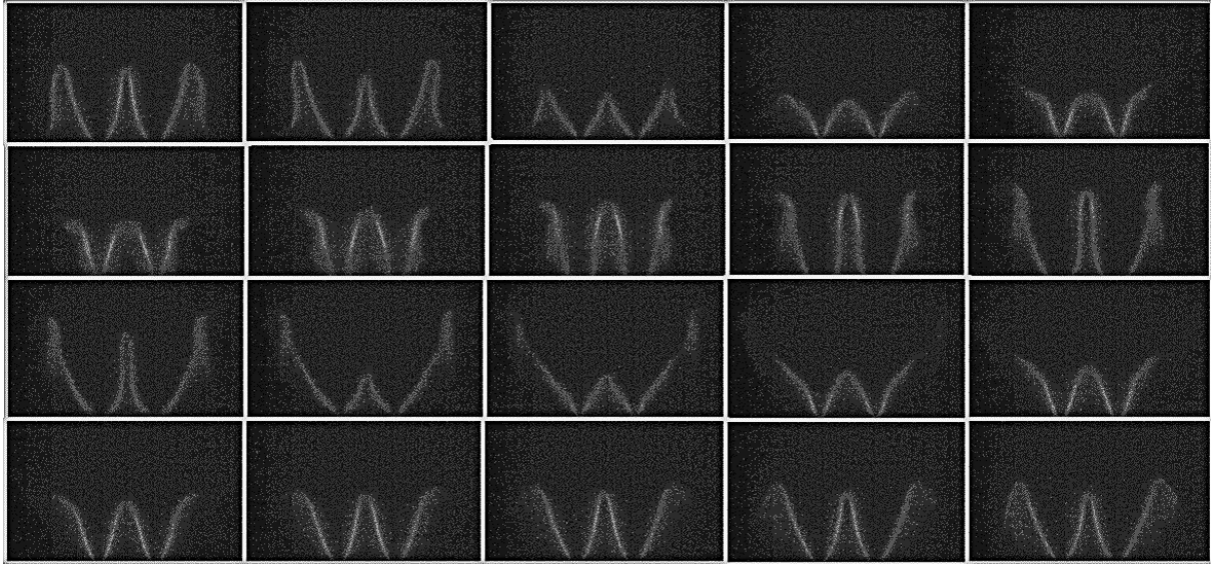


Figure 3.12. Filtered images of the flames during fish-bone instability at 22cm.

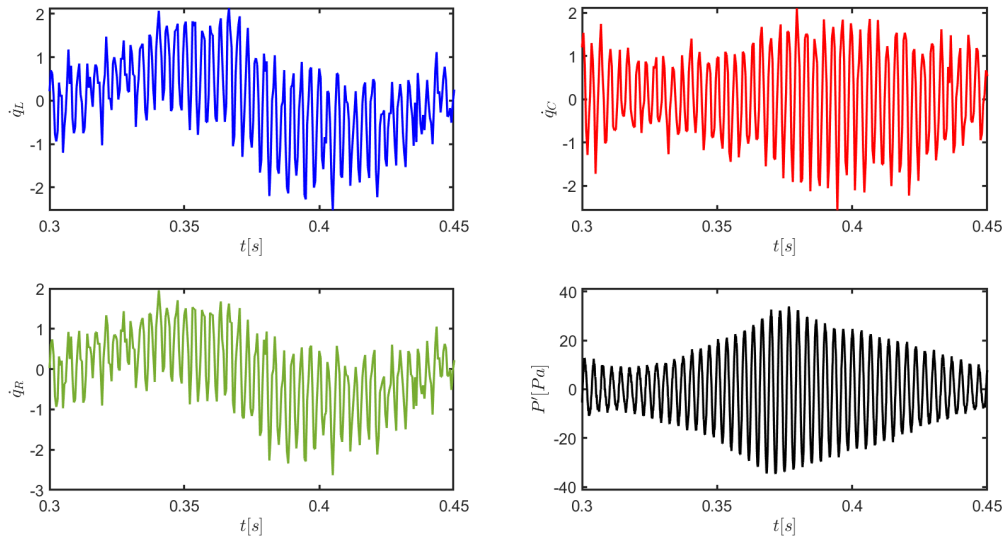


Figure 3.13. Time series of each q' and P' at $x = 22\text{cm}$

This low frequency mode is not present within the PSD of q'_C . This infers that while P' may be strongly synchronized with q'_C , the effects of q'_L and q'_R are still translated into the dynamics of P' . This claim is visually evident in figure 3.12, where the left and right flames are nearly entirely lifted from the burner tip but are anchored by the center flame. The center flame remains fully anchored to the burner tip and experiences oscillatory vibrations of its surface area. The center

flame possesses more surface area compared to the left and right and will therefore possess a higher amplitude during oscillations. The center flame is not as susceptible to pressure waves from the acoustic field and is therefore able to prevent lifting but also support the left and right flames. The image set is for one large amplitude oscillation, which accounts for a single period of the 6.7Hz frequency.

From the image set in figure 3.12 we may observe that the left and right flames may lift enough to reduce the amplitude of \dot{q}' to the surrounding hydrodynamic region. This may dampen the amplitude of P' and allow the flames to re-anchor to the burner tip. When the left and right flames re-anchor, they regain surface area, releasing a higher amplitude of \dot{q}' into the chamber. This restarts the cycle and the P' vibrations increase amplitude, lifting the left and right flames again. This can be observed in the time series of each \dot{q}' and P' in figure 3.13 which focuses on the period of a single "fish-bone" in the P' time series. The amplitudes \dot{q}'_L and \dot{q}'_R reach their maximum at approximately 0.35 seconds, inferring that they must be anchored to the burner. P' however, only reaches its local maximum at approximately 0.37 seconds and \dot{q}'_C seems to do the same. This lag between the left and right flame oscillations and P' shows that \dot{q}'_L and \dot{q}'_R are driving the overall pattern observed in the fish-bone instability. This period corresponds to the frequency of 6.7Hz present in the PSD's of \dot{q}'_L , \dot{q}'_R , and P' . We can therefore infer that \dot{q}'_C may be a stronger influence on the dominant frequency for P' , however, we note that \dot{q}'_L and \dot{q}'_R cause the low frequency fish bone pattern. The complex dynamics of fish-bone instability is therefore heavily influenced by how the different \dot{q}' 's interact with P' .

During periodic oscillations at 70cm, figure 3.14 shows many clear dominant frequencies, with a dominant mode for P' and \dot{q}' 's at 182.5Hz. All three \dot{q}' 's share the exact same frequencies and are therefore responding to P' as a relatively singular \dot{q}' source. The flames do possess a low order 15Hz peak that is not present in the P' PSD. This frequency was observed in the PSD's of \dot{q}'_L , \dot{q}'_R , and \dot{q}'_C for every location but is not present within the P' PSD's, which is shown in the appendix. This frequency may therefore not be a characteristic unique to the periodic oscillations.

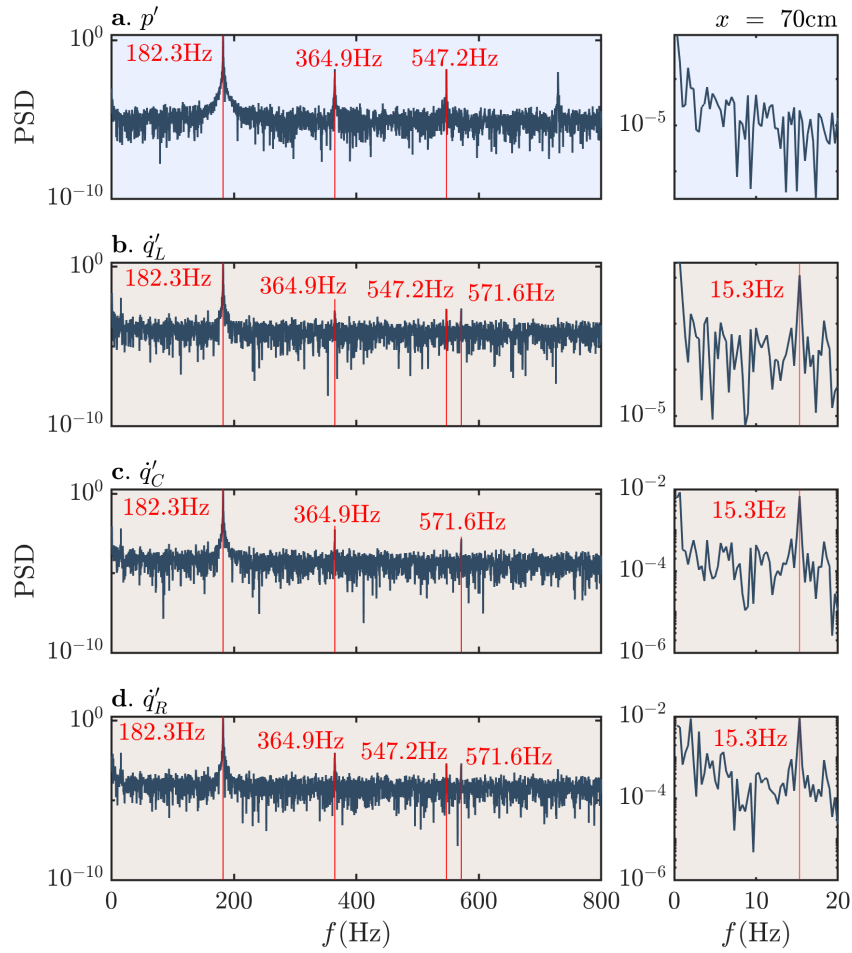


Figure 3.14. PSD's of each q' and P' at $x = 70\text{cm}$

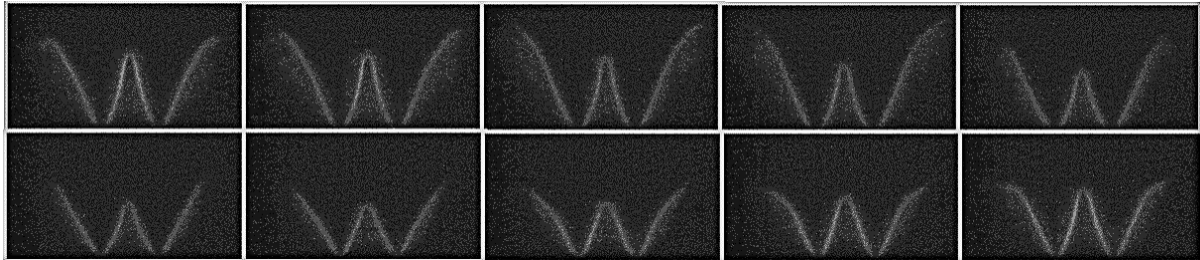


Figure 3.15. Filtered images of the flames during limit cycle oscillations at 70cm.

Unlike fish-bone instability, the periodic oscillations continue a consistent pattern seen in figure 3.15. The time series of each q' and P' are also very similar, lacking any large amplitude oscillations at a low order frequency in figure 3.16. Each q' is oscillating at the same rate and while the P' time series are not perfectly periodic, this location within the Rijke tube presents a

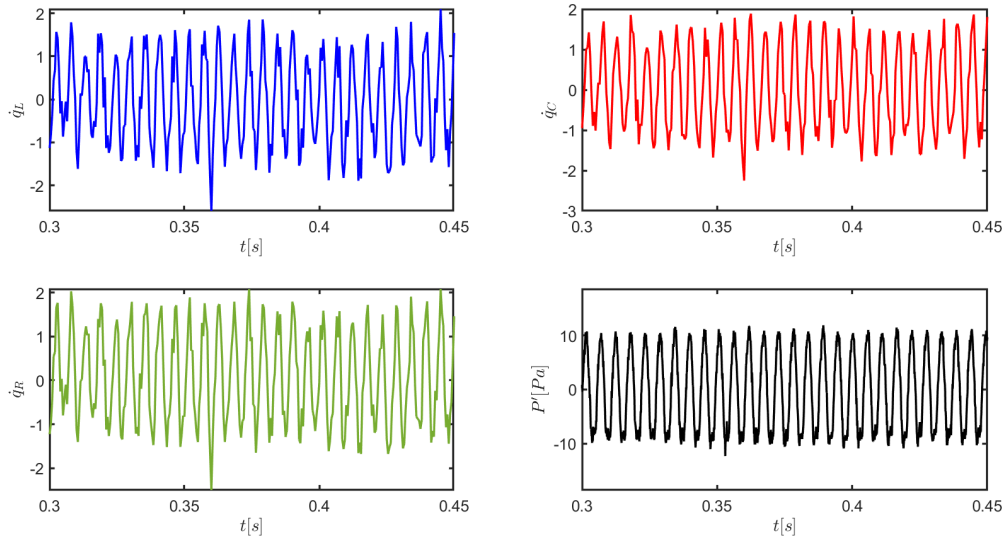


Figure 3.16. Time series of each \dot{q}' and P' at $x = 70\text{cm}$

much simpler dynamical state when compared to the fish-bone instability.

From figures 3.11 and 3.14 we may observe that the individual \dot{q}' oscillations will translate into the P' dynamics, whether the flames are synchronized or not. The fish-bone instability is a key representation of how the individual \dot{q}' 's may affect the acoustic field separately. The outer flames lifting due to the acoustic field and reigniting from the center flame may be the cause for the overall pattern that is characteristic of fish-bone instability. This comparison provides a key example as to how complex dynamics observed in P' may stem from the varying influences from each flame during thermoacoustic instability of multi-flame burners.

3.2.5 Asymmetrical Three Flame Experiment

The susceptibility of the flames to the affects of the pressure oscillations will also influence the observed dynamics within the acoustic pressure field during thermoacoustic instability. When comparing the 3HL burner tip to the 3HT burner tip, the overall dynamics changed dramatically. The 3HT experiment experienced an initial bifurcation point at 18cm, moving directly to a quasi-periodic regime which is observed in figure 3.17. Then the flame blew out at 19cm with multiple attempts to reignite and move past the location. The early blow-off and

higher amplitude range of the asymmetrical case could be due to how all three flames are equally susceptible to the acoustic pressure field and lack a center flame to anchor to.

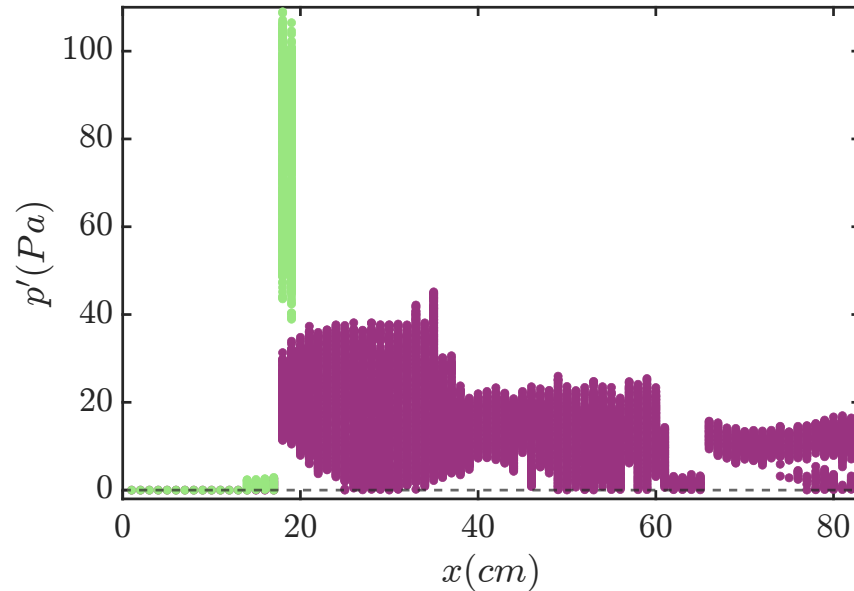


Figure 3.17. Bifurcation plot of P' for the asymmetrical(green) and in-line(purple) burner tip experiments

This is a major difference compared to the in-line case which, as observed in the previous section, did not blow off for the length of the Rijke tube. The amplitude of the asymmetrical case was nearly twice that of the in-line experiment at 120Pa shown in figure 3.17. There are also multiple different frequencies present in the PSD of 19cm whereas the in-line case has dominant peaks of 300Hz and 5Hz.

Figure 3.18 compares the P' time series data between the 3HL and 3HT experiments at 19cm. Unlike the 3HL experiment, the 3HT case did not possess clear fish-bone instability within the time series but does show amplitude modulate as seen in figure 3.18. The PSD of the 3HT case also shows many more obvious peaks in a range of frequencies spanning from 100 to 1000Hz whereas the 3HL experiment only contained a low order and three related higher order peaks.

The difference of the observed dynamical states in P' for each case lies in the burner configuration. The 3HL tip prevents the center flame from lifting due to the left and right flames.

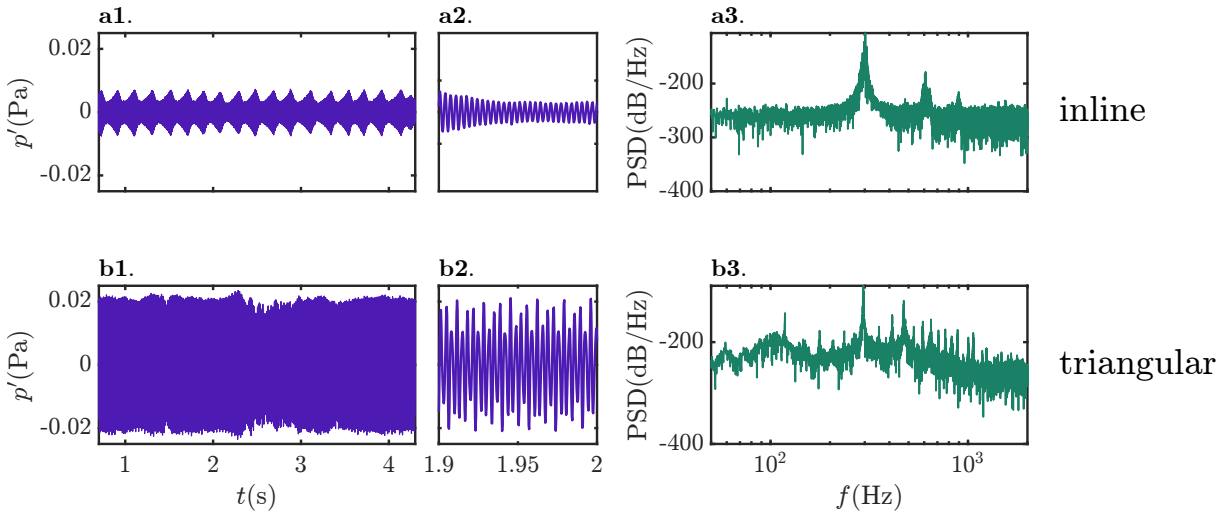


Figure 3.18. P' signal and PSD of the in-line(top) and asymmetrical(bottom) three flame burner experiments at 19cm in the Rijke.

This evidently creates a more stable burner due to the observed lower amplitudes in P' . The 3HT tip does not possess this feature and all three flames are susceptible to the acoustic pressure oscillations. There is also no centralized flame to re-ignite or anchor the exposed flames, making it an inherently less stable design. Because all three flames may interact directly with the pressure field in the chamber, the \dot{q}' may fluctuate at a larger amplitude compared to the 3HL case as there is more flame surface area directly exposed to the surrounding flow. This may therefore allow the three \dot{q}' sources to act as individual oscillators with P' , potentially developing a more complex system.

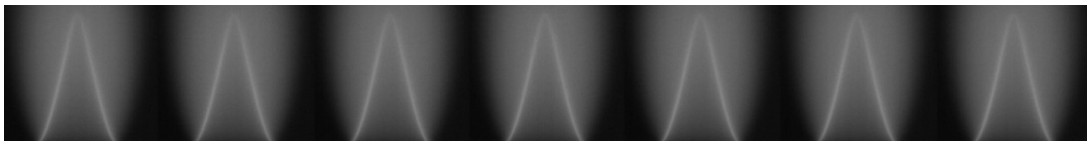


Figure 3.19. Steady State Flame on the 1H tip



Figure 3.20. Unstable flames on the 7H tip

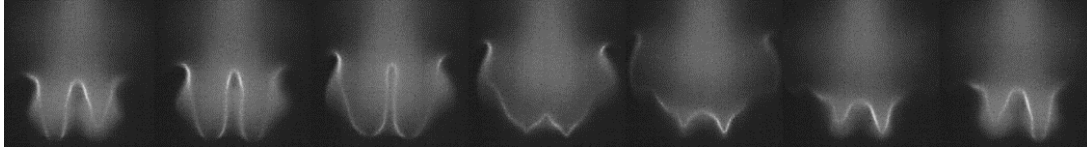


Figure 3.21. Unstable flames on the 3HL 3-flame tip

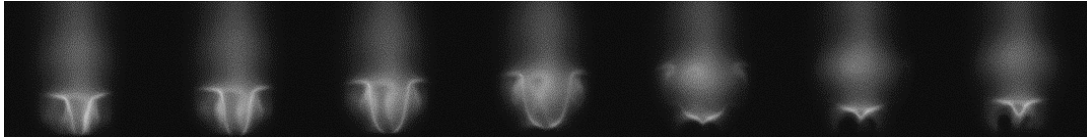


Figure 3.22. Unstable flames on the 3HT tip

Figures 3.19, 3.20, 3.21, and 3.22 compare each burner tip during their relevant experiments. The 7H image set shows the flames lifting and reigniting as one, however, the outer ring clearly blows off nearly half of the flame front whereas the center flame seems to breakup in figure 3.20. It can be observed in the 3HL image set in figure 3.21 that the left and right flames are lifted and there could even be a slight lag between lift and re-ignition. The center flame anchors the outer flames onto the tip. The image set starts with the right flame blowing off, but is anchored to the burner tip from the center flame. Then, in the fourth image from the right, the left flame begins lifting in a similar manner.

The 3HT image set in figure 3.22 shows that all three flames oscillate with an in-phase pattern. The three flames lift and reignite at the same time, possessing similar shapes in every frame. Unlike the in the 3HL and 7H cases, there is no center flame to anchor the outer flames when the lift from the burner tip. Which again could have been a reason why the 3HT experiment experienced complete blow-off very early when moving down the Rijke tube.

Chapter 4

Conclusion and future work

4.1 Conclusion

In this study, an experimental setup using a Rijke tube was developed to study thermoacoustic instability of a laminar, premixed flame. The Rijke tube dimensions were sized to achieve synchronization between the chamber's acoustic pressure and the flame that acts as a heat source. Pressure sensors and a high speed camera were selected and tested for collecting data on the acoustic pressure as well as heat release rate of the flame.

A systematic experiment was conducted on four different burner tips by collecting pressure and heat release rate data. By changing the amount of flames and their layout, the recorded dynamics of acoustic pressure changed dramatically. We compared the pressure bifurcation plots of single, seven, and three flame experiments, noting how the range of amplitudes changed across each case. The heat release rate and synchronization to the pressure field were further investigated for the in-line three flame case.

By performing an analysis on the synchronization between the three individual \dot{q}' data and P' , we found that the phase lock value differed for the different dynamic states observed in P' across the length of the Rijke tube. As the dynamics of P' transitioned from fish-bone instability to mixed mode and burst mode, the individual PLV and RMF values dropped and varied dramatically when compared to the periodic state, where all flames were in phase. Furthermore, when investigating a representative location during fish-bone instability we found that the \dot{q}'

PSD's differed between \dot{q}'_L , \dot{q}'_C , and \dot{q}'_R and each one had different frequency peaks that matched the dominant modes observed in the P' PSD's at the respective locations. This supports the notion that each \dot{q}' contributed in varying degrees to the observed P' dynamics during more complex dynamics such as fish-bone instability, mixed-mode, and burst mode.

An asymmetrical three-flame burner tip was also tested and the recorded P' was compared to the in-line three flame data set. Even with the same flame conditions, the asymmetrical case blew off after a short duration within the Rijke tube. The asymmetrical tip exposed each flame to the acoustic pressure field equally and lacked any centralized flame. The amplitude was much larger for the 3HT case potentially due to how all 3 flames could respond to the acoustic perturbations. Regardless of the dynamical state of the P' data, each \dot{q}' will interact with the pressure during thermoacoustic instability. In this work, the single flame did not produce any complex dynamics that the multi-flame burners did. This fundamental structure observed within this work supports that the configuration of the flames on a burner will greatly affect the dynamics of P' during thermoacoustic instability. This systematic study of the effect of multi-flame burners on thermoacoustic instability concludes that configuration of the flames within a combustion device may dramatically influence the observed dynamics during the onset of thermoacoustic instability.

4.2 Future Work

In this work, four burner tip configurations were investigated and their observed pressure dynamics were compared for laminar, premixed flames. The heat release rate of the in-line three flame burner was analyzed in the context of the corresponding pressure data to further understand the affect of mulit-flame burners on thermoacoustic instability. To more precisely study the underlying physics of how flame-flame interactions affect combustion instability, more data must be collected on a variety of configurations and burner types. The \dot{q}' data collected by a high speed camera was confined to a single planar view and may only record up to 2000fps.

This was a limitation to our experimental setup and could may be mitigated with a more precise camera or the utilization of multiple cameras.

Additionally, the introduction of particle tracking may also allow for more accurate \dot{q}' data collection. This would allow for higher fps recordings as well as the study of turbulent flames. This could also allow for the study of local flame dynamics within single flame-lets as well as local interactions between the flames. The additional perspectives obtained could provide more accurate data to further understand the physics of local flame interactions during the onset of thermoacoustic instability.

4.3 Appendix

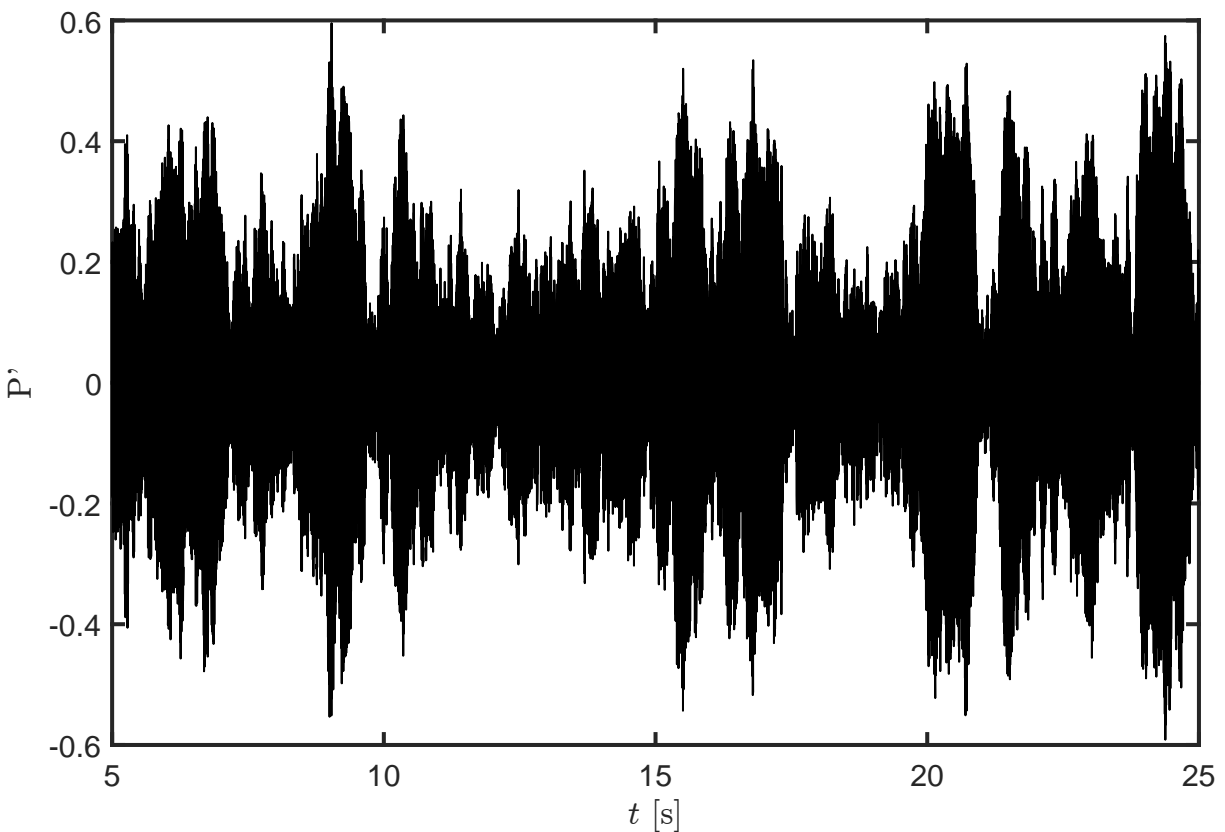


Figure 4.1. Normalized P' from the 50.8 mm diameter Rijke tube

The normalized P' data taken during thermoacoustic instability is shown in figure 4.1. This was during development of the Rijke tube setup from section 3.1.

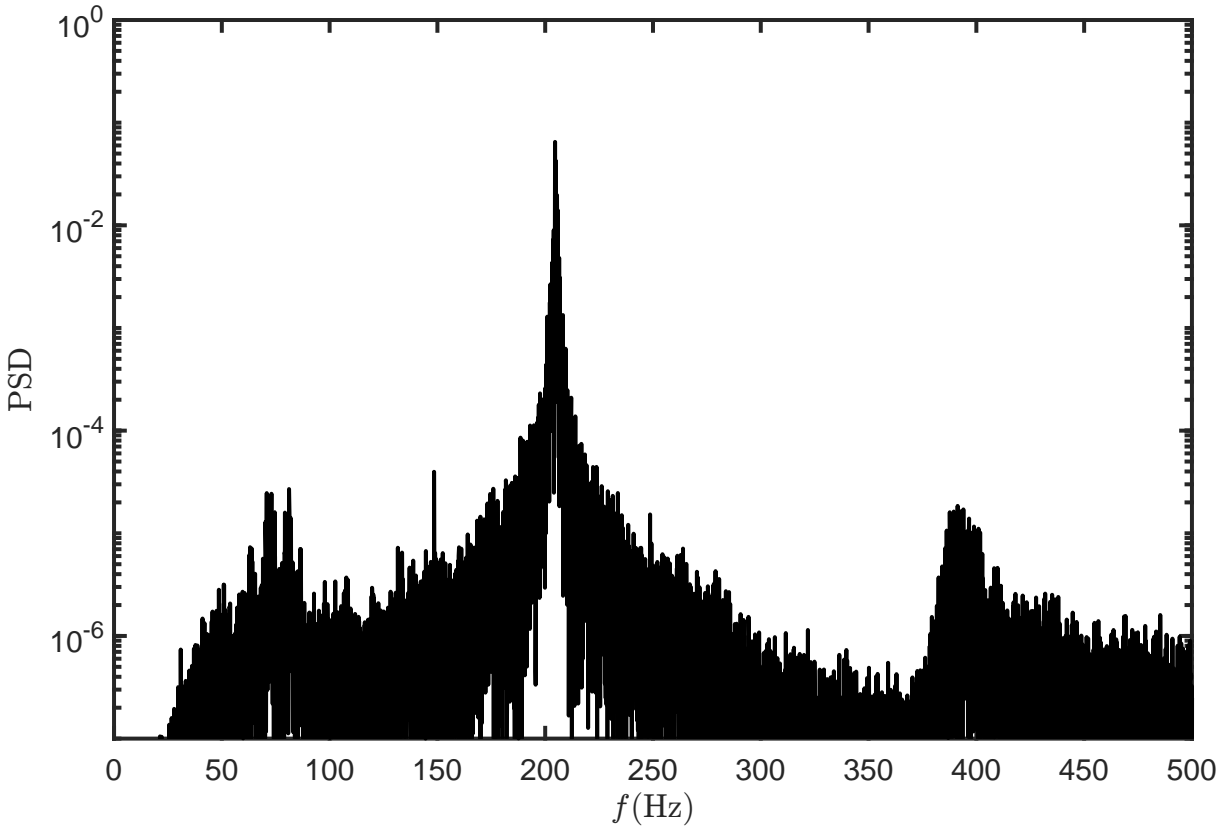


Figure 4.2. PSD of P' from the 50.8mm diameter Rijke tube

Figure 4.2 shows the dominant frequencies from the P' time series in figure 4.1 during Rijke tube setup development in section 3.1.

Figure 4.3 is from section 2.2 showing the background noise of the setup without a flame. Its maximum recorded amplitude is just under 5Pa.

The pressure sensors were tested with a signal generator in section 2.2. Figure 4.4 shows how the sensors were setup during these tests.

Figure 4.5 shows the time series of the P' each sensor read during calibration tests in section 2.2. Both were mostly in phase during the test.

Figure 4.6 shows the PSD of the P' each sensor read during calibration tests in section 2.2. Both are exactly 750Hz.

Fig 4.7 shows the time series of each q' and P' for 3 seconds at 22cm. This data was analyzed during section 3.2.3.

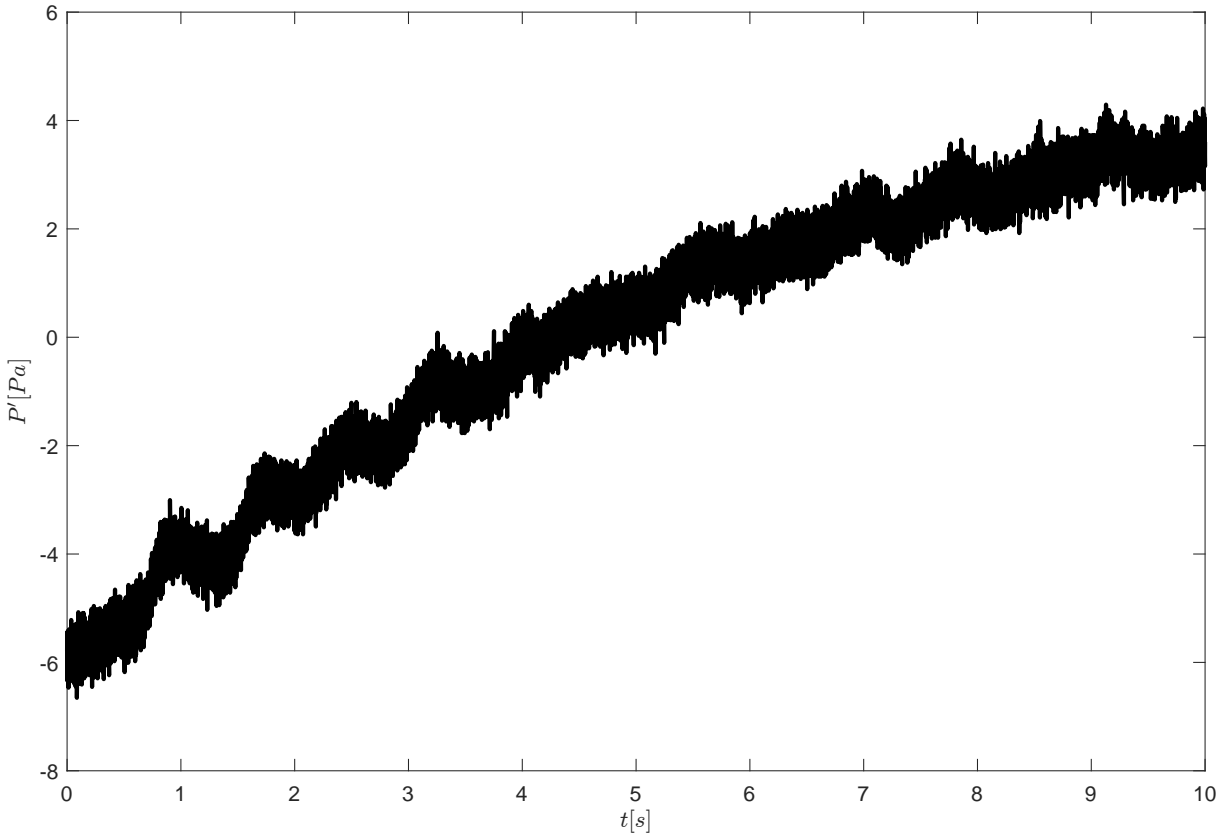


Figure 4.3. Background noise of the setup recorded from the bottom pressure sensor

Fig 4.8 shows the PSD of each \dot{q}' and P' at 22cm. This data was analyzed during section 3.2.3.

Fig 4.9 shows the time series of each \dot{q}' and P' for 3 seconds at 33cm. This data was analyzed during section 3.2.3.

Fig 4.10 shows the PSD of each \dot{q}' and P' at 33cm. This data was analyzed during section 3.2.3.

Fig 4.11 shows the time series of each \dot{q}' and P' for 3 seconds at 46cm. This data was analyzed during section 3.2.3.

Fig 4.12 shows the PSD of each \dot{q}' and P' at 46cm. This data was analyzed during section 3.2.3.

Fig 4.13 shows the time series of each \dot{q}' and P' for 3 seconds at 59cm. This data was analyzed during section 3.2.3.

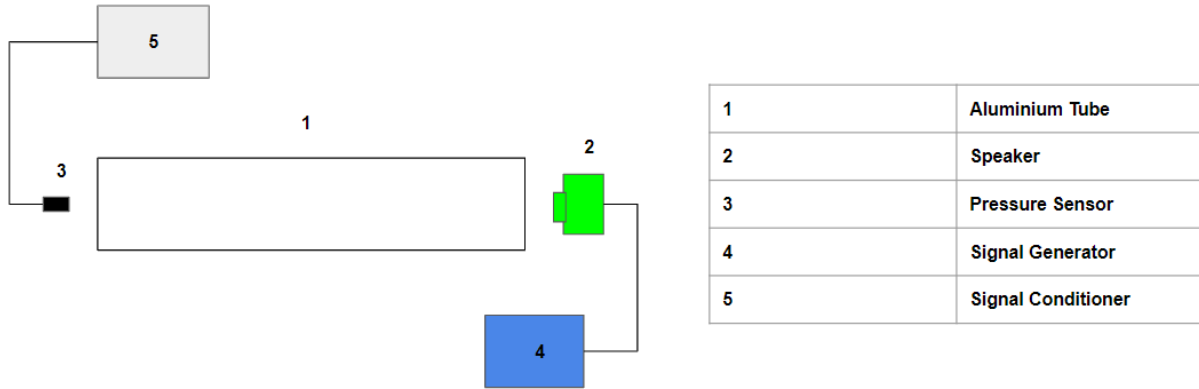


Figure 4.4. Pressure Sensor sound test setup diagram

Fig 4.14 shows the PSD of each \dot{q}' and P' at 59cm. This data was analyzed during section 3.2.3.

Fig 4.15 shows the time series of each \dot{q}' and P' for 3 seconds at 70cm. This data was analyzed during section 3.2.3.

Fig 4.16 shows the PSD of each \dot{q}' and P' at 70cm. This data was analyzed during section 3.2.3.

Figure 4.17 plots the False Nearest Neighbor vs amount of dimensions for P' in locations 22cm, 33cm, 46cm, 59cm, and 70cm in section 3.2.2. The minimum dimensions required to prevent false crossing of the trajectories is 5.

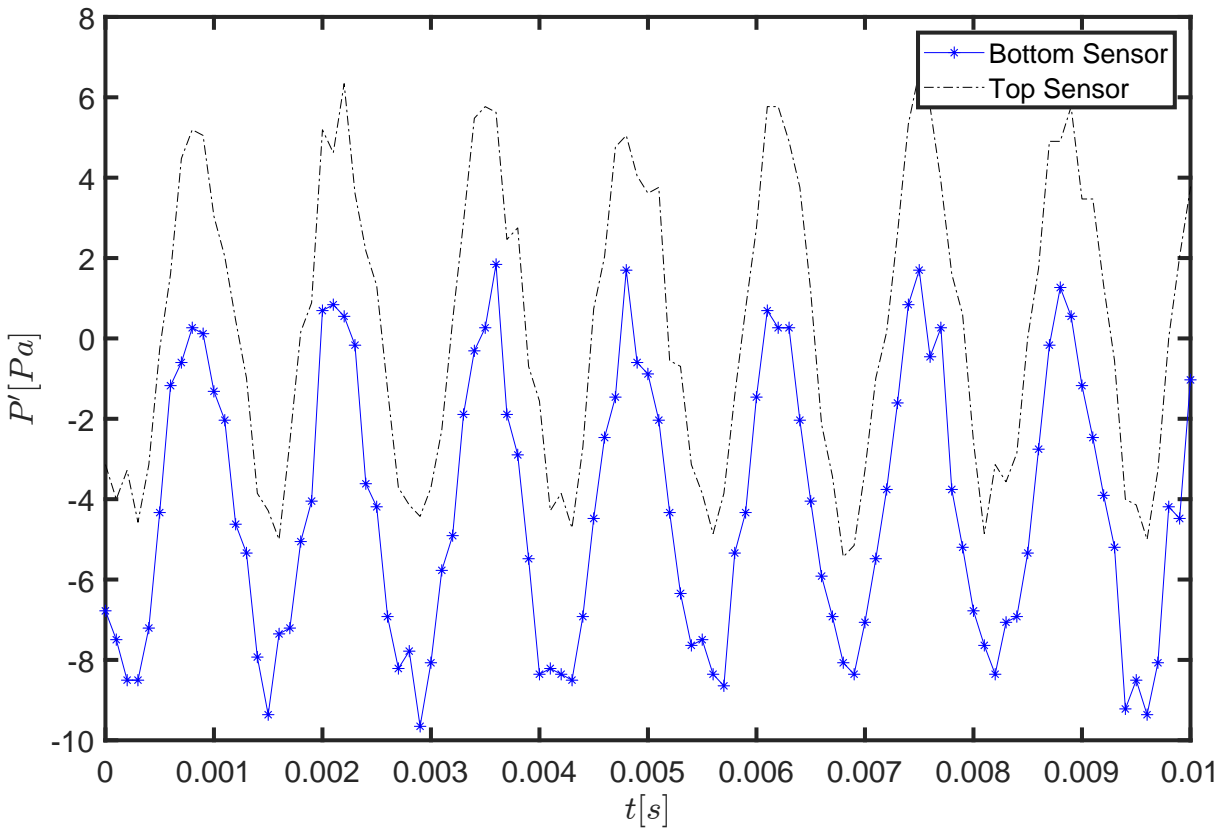


Figure 4.5. Top and Bottom Pressure Sensor Calibration Test Data

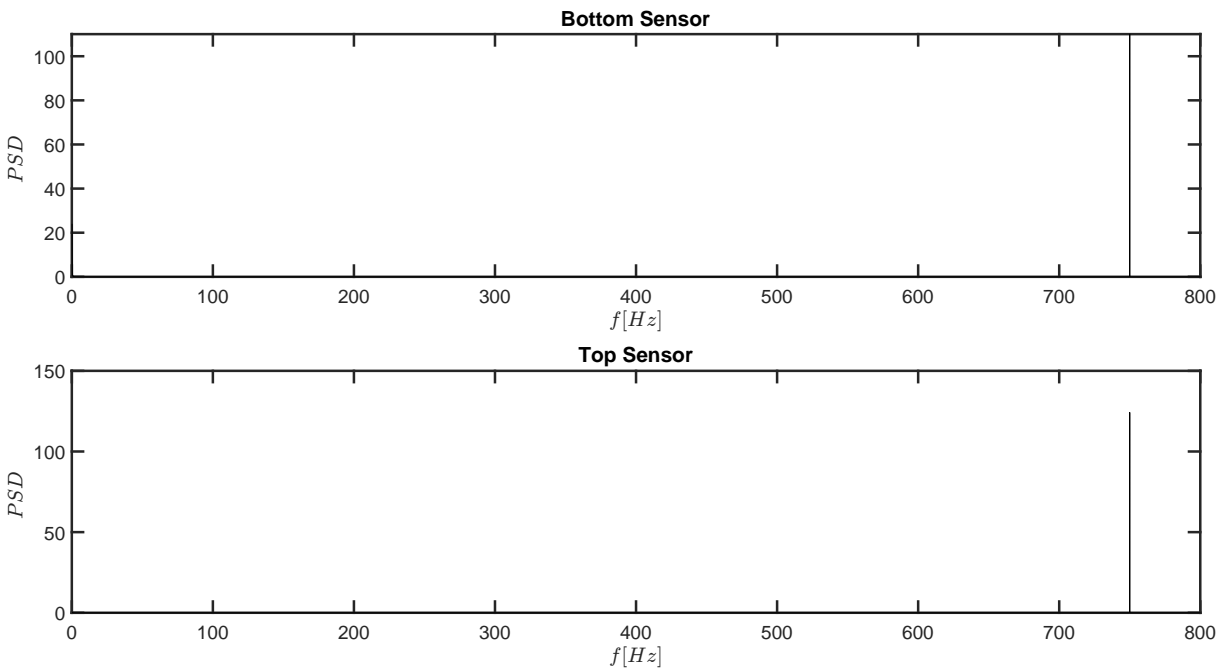


Figure 4.6. Top and Bottom Pressure Sensor Calibration Test PSD's.

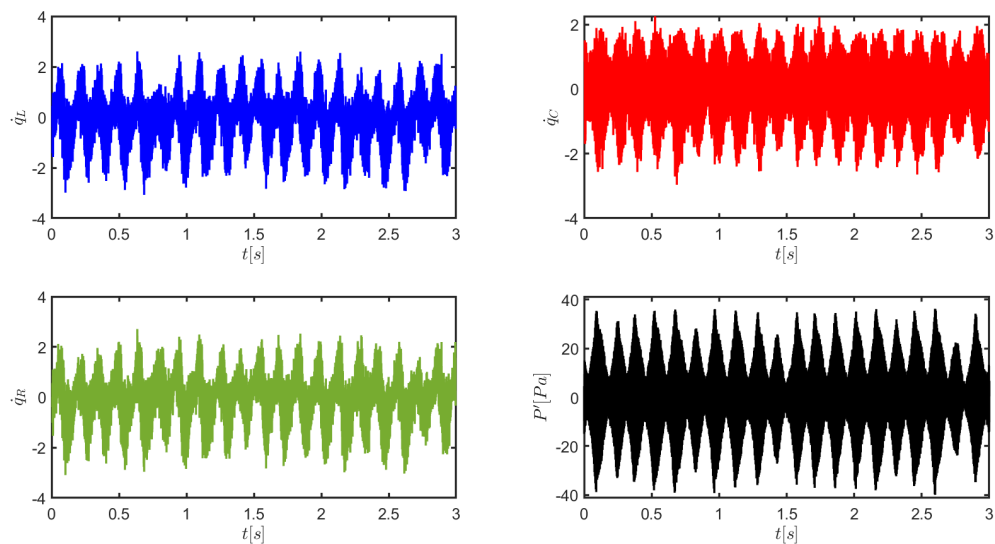


Figure 4.7. Time series data of each \dot{q}' and P' during fish-bone instability at 22cm.

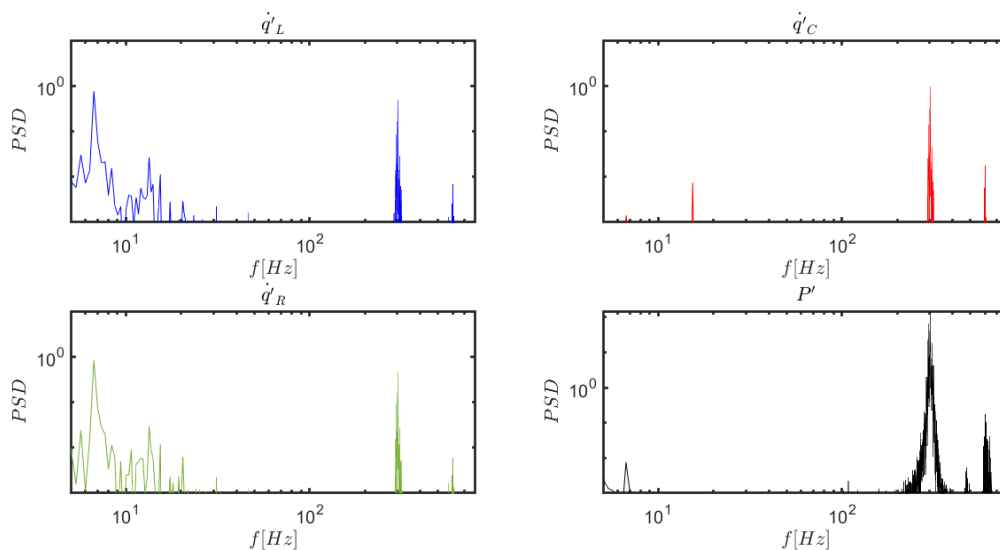


Figure 4.8. PSD's of each \dot{q}' and P' during fish-bone instability at 22cm

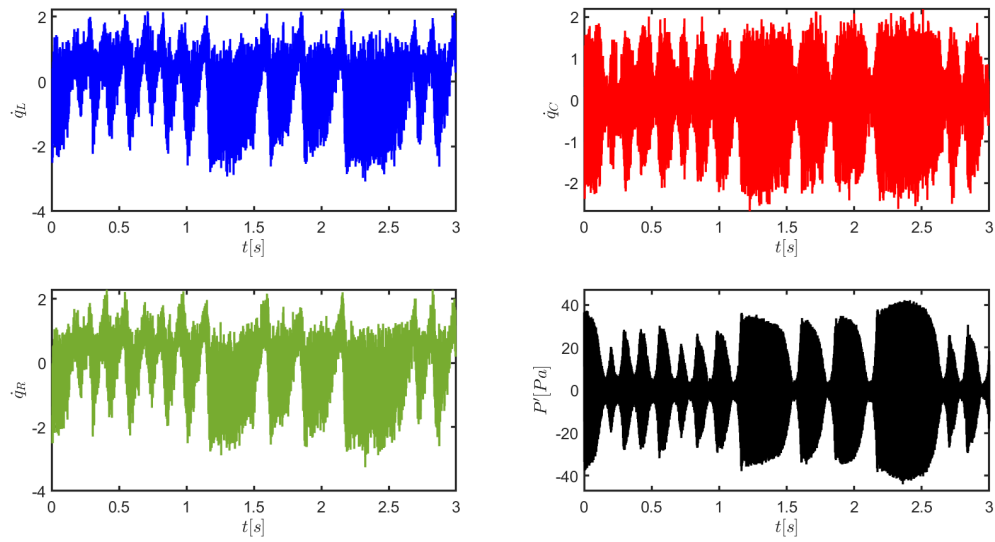


Figure 4.9. Time series data of each \dot{q}' and P' during mixed-mode instability at 33cm.

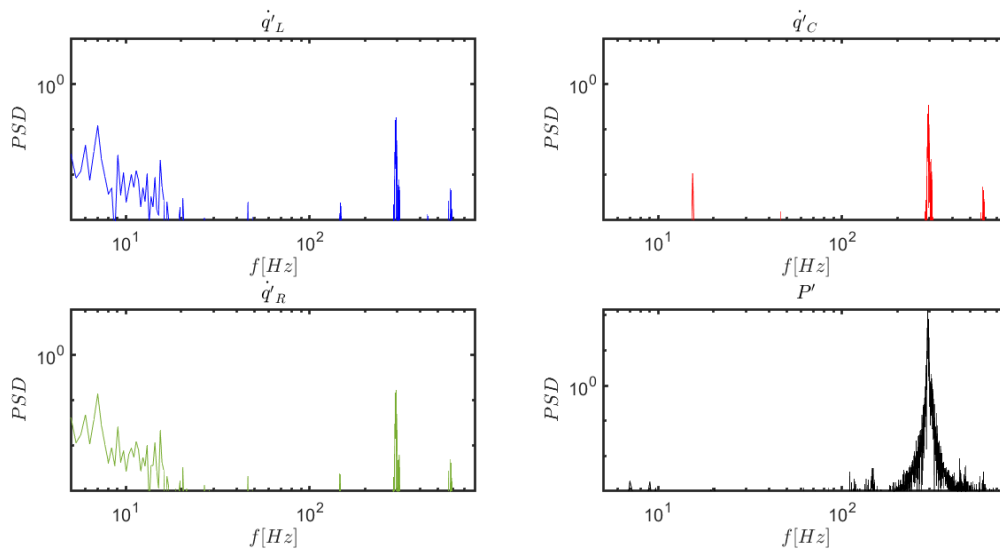


Figure 4.10. PSD's of each \dot{q}' and P' during mixed-mode instability at 33cm

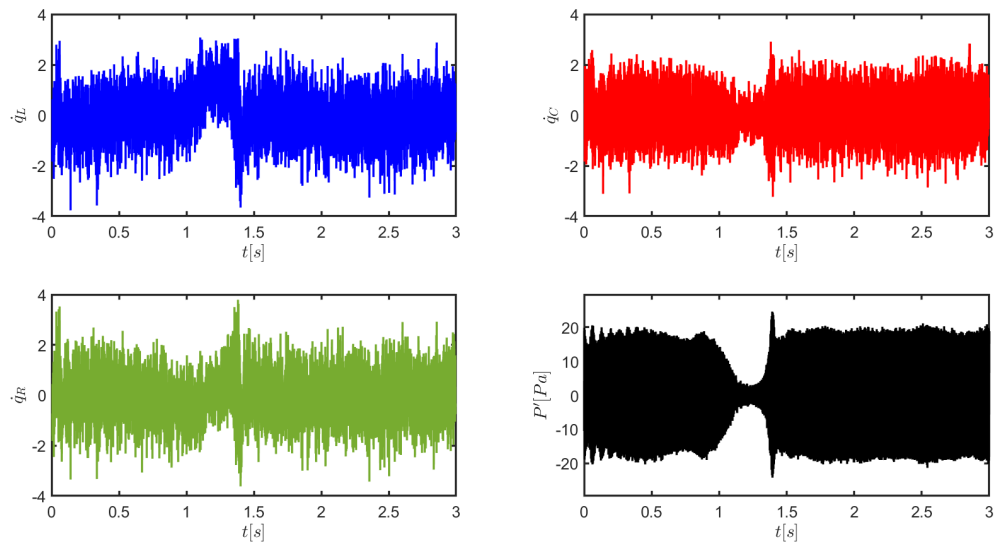


Figure 4.11. Time series data of each \dot{q}' and P' during mixed-mode instability at 46cm.

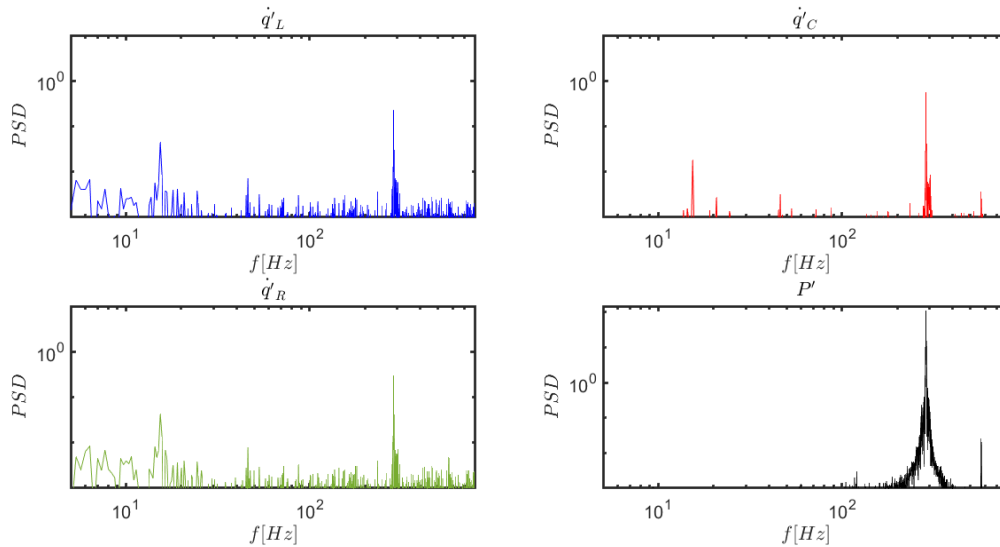


Figure 4.12. PSD's of each \dot{q}' and P' during mixed-mode instability at 46cm

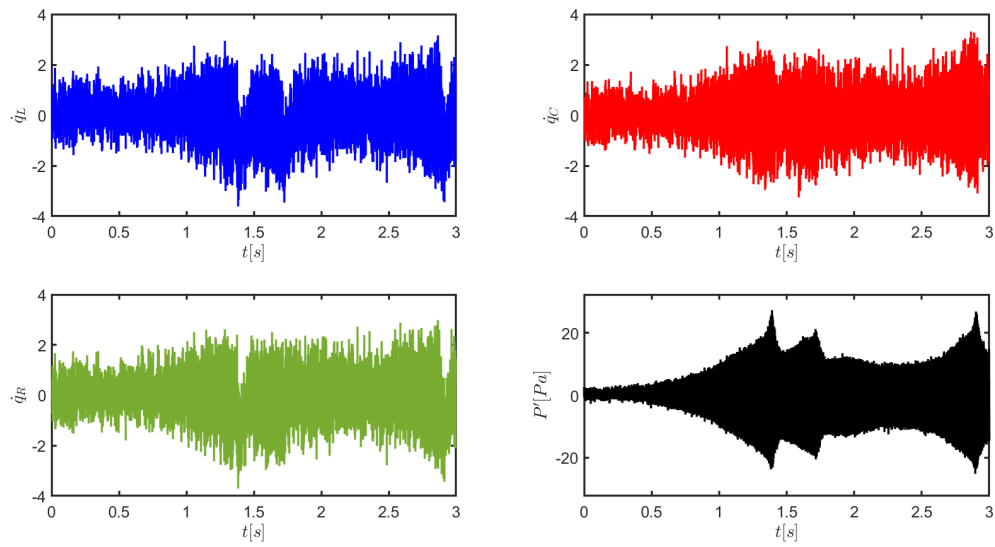


Figure 4.13. Time series data of each \dot{q}' and P' during burst-mode instability at 59cm.

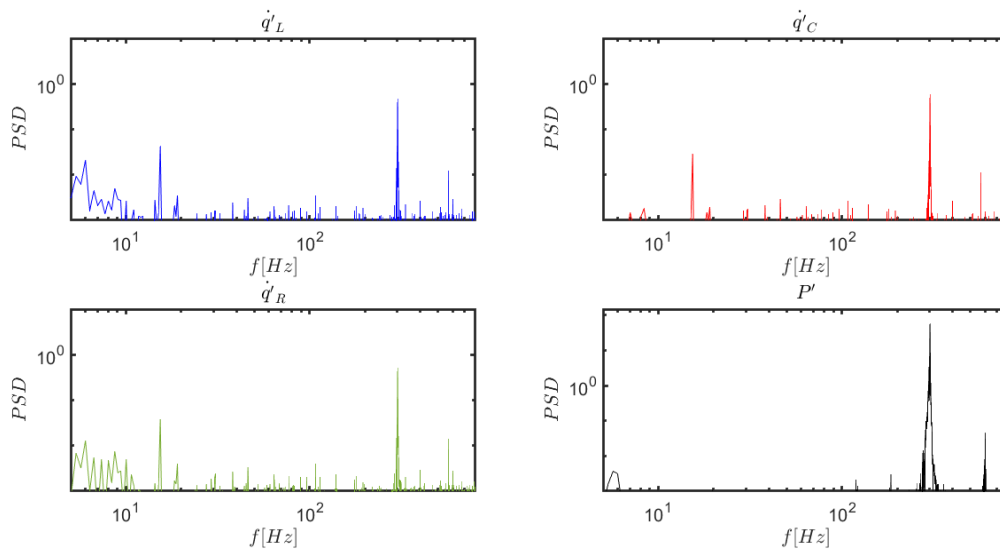


Figure 4.14. PSD's of each \dot{q}' and P' during burst-mode instability at 59cm

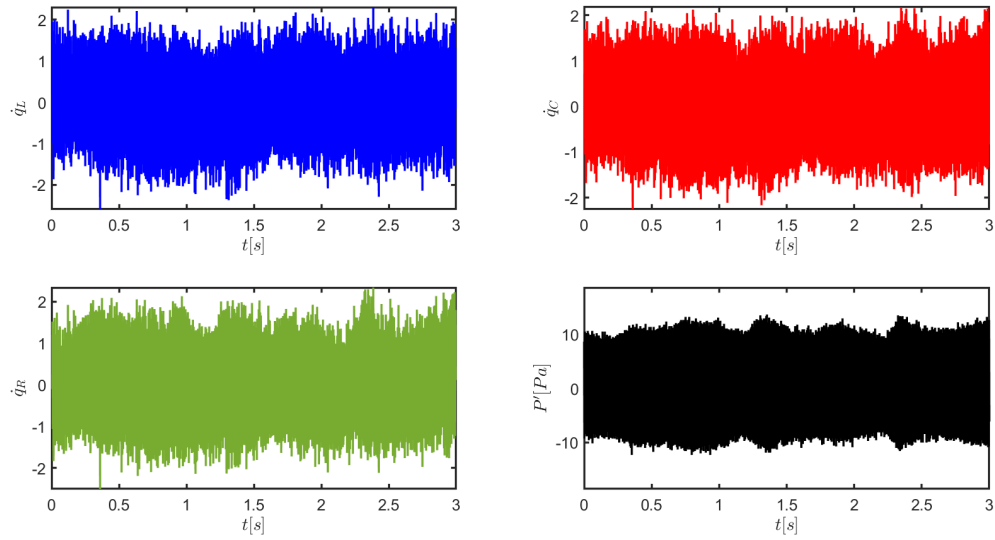


Figure 4.15. Time series data of each \dot{q}' and P' during limit cycle oscillations at 70cm.

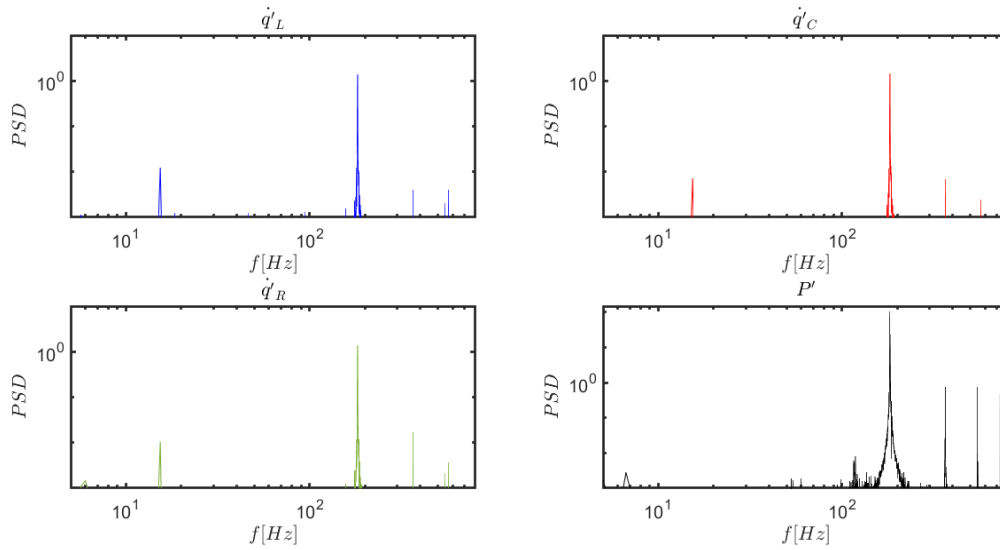


Figure 4.16. PSD's of each \dot{q}' and P' during limit cycle oscillations at 70cm

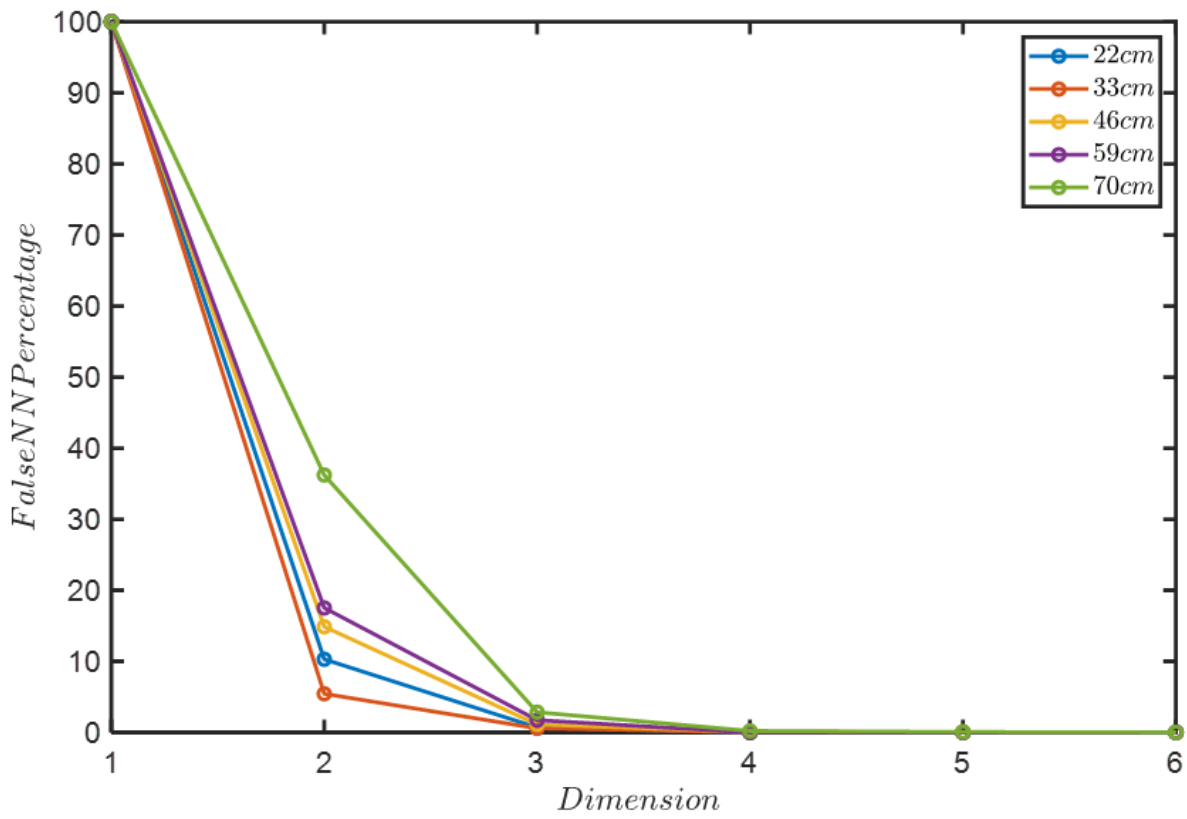


Figure 4.17. Minimum dimensions required to prevent false trajectory crossings for each location

Bibliography

- [1] RI Sujith and Samadhan A Pawar. *Thermoacoustic instability: A complex systems perspective*. Springer Nature, 2021.
- [2] Tim C Lieuwen. Experimental investigation of limit-cycle oscillations in an unstable gas turbine combustor. *Journal of Propulsion and Power*, 18(1):61–67, 2002.
- [3] Vigor Young. *Liquid rocket engine combustion instability*, volume 169. Aiaa, 1995.
- [4] Luigi Crocco, Jerry Grey, and David T Harrje. Theory of liquid propellant rocket combustion instability and its experimental verification. *ARS Journal*, 30(2):159–168, 1960.
- [5] Fred EC Culick. Combustion instabilities in liquid-fuelled propulsion systems. 1988.
- [6] M Barrere and FA Williams. Comparison of combustion instabilities found in various types of combustion chambers. In *Symposium (International) on Combustion*, volume 12, pages 169–181. Elsevier, 1969.
- [7] Timothy C Lieuwen and Vigor Yang. *Combustion instabilities in gas turbine engines: operational experience, fundamental mechanisms, and modeling*. American Institute of Aeronautics and Astronautics, 2005.
- [8] Annafederica Urbano, Quentin Douasbin, Laurent Selle, Gabriel Staffelbach, Bénédicte Cuenot, Thomas Schmitt, Sébastien Ducruix, and Sébastien Candel. Study of flame response to transverse acoustic modes from the les of a 42-injector rocket engine. *Proceedings of the Combustion Institute*, 36(2):2633–2639, 2017.
- [9] YC Yu, JC Sisco, V Sankaran, and WE Anderson. Effects of mean flow, entropy waves, and boundary conditions on longitudinal combustion instability. *Combustion Science and Technology*, 182(7):739–776, 2010.
- [10] Lord Rayleigh. The explanation of certain acoustical phenomena. *Roy. Inst. Proc.*, 8:536–542, 1878.
- [11] Abbott A Putnam and William R Dennis. Organ-pipe oscillations in a burner with deep

- ports. *The Journal of the Acoustical Society of America*, 28(2):260–269, 1956.
- [12] Perry L Blackshear Jr. Driving standing waves by heat addition. Technical report, 1952.
- [13] FEC Culick. Non-linear growth and limiting amplitude of acoustic oscillations in combustion chambers. *Combustion Science and Technology*, 3(1):1–16, 1971.
- [14] AA Peracchio and WM Proscia. Nonlinear heat-release/acoustic model for thermoacoustic instability in lean premixed combustors. In *Turbo Expo: Power for Land, Sea, and Air*, volume 78644, page V003T06A022. American Society of Mechanical Engineers, 1998.
- [15] Vigor Yang and FRED CULICK. Third-order nonlinear acoustic waves and triggering of pressure oscillations in combustion chambers. i-longitudinal modes. In *23rd Joint Propulsion Conference*, page 1873, 1987.
- [16] A Fichera, C Losenno, and A Pagano. Experimental analysis of thermo-acoustic combustion instability. *Applied Energy*, 70(2):179–191, 2001.
- [17] Lipika Kabiraj and RI Sujith. Nonlinear self-excited thermoacoustic oscillations: intermittency and flame blowout. *Journal of Fluid Mechanics*, 713:376–397, 2012.
- [18] Tim Lieuwen and Ben T Zinn. The role of equivalence ratio oscillations in driving combustion instabilities in low nox gas turbines. In *Symposium (International) on combustion*, volume 27, pages 1809–1816. Elsevier, 1998.
- [19] Chee Su Goh and Aimee S Morgans. The influence of entropy waves on the thermoacoustic stability of a model combustor. *Combustion Science and Technology*, 185(2):249–268, 2013.
- [20] Jan Kopitz and Wolfgang Polifke. Cfd-based application of the nyquist criterion to thermoacoustic instabilities. *Journal of Computational Physics*, 227(14):6754–6778, 2008.
- [21] C-C Hantschk and D Vortmeyer. Numerical simulation of self-excited thermoacoustic instabilities in a rijke tube. *Journal of Sound and Vibration*, 227(3):511–522, 1999.
- [22] Sébastien Candel. Combustion dynamics and control: Progress and challenges. *Proceedings of the Combustion Institute*, 29(1):1 – 28, 2002. Proceedings of the Combustion Institute.
- [23] Benjamin D Bellows, Mohan K Bobba, Jerry M Seitzman, and Tim Lieuwen. Nonlinear flame transfer function characteristics in a swirl-stabilized combustor. 2007.
- [24] M. A. Macquisten, M. Whiteman, S. R. Stow, and A. J. Moran. Exploitation of measured flame transfer functions for a two-phase lean fuel injector to predict thermoacoustic modes in full annular combustors. volume Volume 4A: Combustion, Fuels and Emissions of *Turbo*

Expo: Power for Land, Sea, and Air, 06 2014.

- [25] Daesik Kim, Jong Guen Lee, Bryan D Quay, Domenic A Santavicca, Kwanwoo Kim, and Shiva Srinivasan. Effect of flame structure on the flame transfer function in a premixed gas turbine combustor. *Journal of Engineering for Gas Turbines and Power*, 132(2), 2010.
- [26] WS Cheung, GJM Sims, RW Copplesstone, JR Tilston, CW Wilson, Simon R Stow, and Ann P Dowling. Measurement and analysis of flame transfer function in a sector combustor under high pressure conditions. In *Turbo Expo: Power for Land, Sea, and Air*, volume 36851, pages 187–194, 2003.
- [27] Kyu Tae Kim, Jong Guen Lee, BD Quay, and DA Santavicca. Spatially distributed flame transfer functions for predicting combustion dynamics in lean premixed gas turbine combustors. *Combustion and Flame*, 157(9):1718–1730, 2010.
- [28] Florent Duchaine and Thierry Poinso. Sensitivity of flame transfer functions of laminar flames. In *Proceedings of the Summer Program*, page 251, 2010.
- [29] M Fleifil, Anuradha M Annaswamy, ZA Ghoneim, and Ahmed F Ghoniem. Response of a laminar premixed flame to flow oscillations: A kinematic model and thermoacoustic instability results. *Combustion and flame*, 106(4):487–510, 1996.
- [30] Thierry Schuller, Sébastien Ducruix, Daniel Durox, and Sébastien Candel. Modeling tools for the prediction of premixed flame transfer functions. *Proceedings of the Combustion Institute*, 29(1):107–113, 2002.
- [31] A. P. Dowling. Nonlinear self-excited oscillations of a ducted flame. *Journal of Fluid Mechanics*, 346:271–290, 1997.
- [32] A. P. Dowling. A kinematic model of a ducted flame. *Journal of Fluid Mechanics*, 394:51–72, 1999.
- [33] Nicolas Noiray, Daniel Durox, Thierry Schuller, and Sébastien Candel. A unified framework for nonlinear combustion instability analysis based on the flame describing function. *Journal of Fluid Mechanics*, 615:139–167, 2008.
- [34] Arthur F. Gelb and Wallace E. Vander Velde. Multiple-input describing functions and nonlinear system design. pages 137–139, 1968.
- [35] Matthew P. Juniper and R I Sujith. Sensitivity and nonlinearity of thermoacoustic oscillations. *Annual Review of Fluid Mechanics*, 50(1):661–689, 2018.
- [36] Yue Weng, Vishnu R Unni, RI Sujith, and Abhishek Saha. Synchronization framework for modeling transition to thermoacoustic instability in laminar combustors. *Nonlinear*

- Dynamics*, 100(4):3295–3306, 2020.
- [37] S Mondal, SA Pawar, and RI Sujith. Synchronous behaviour of two interacting oscillatory systems undergoing quasiperiodic route to chaos. *Chaos: An Interdisciplinary Journal of Nonlinear Science*, 27(10):103119, 2017.
- [38] Yue Weng, Vishnu R Unni, RI Sujith, and Abhishek Saha. Synchronization based model for turbulent thermoacoustic systems. *arXiv preprint arXiv:2206.05663*, 2022.
- [39] Krishna Manoj, Samadhan A Pawar, and RI Sujith. Experimental investigation on the susceptibility of minimal networks to a change in topology and number of oscillators. *Physical Review E*, 103(2):022207, 2021.
- [40] K Thomas Feldman Jr. Review of the literature on rijke thermoacoustic phenomena. *Journal of Sound and Vibration*, 7(1):83–89, 1968.
- [41] Xiaoling Chen, Evan Dillen, Hosam Fathy, and Jacqueline O’Connor. Optimizing the design of a rijke tube experiment for combustion stability model identifiability. In *2019 American Control Conference (ACC)*, pages 4974–4981. IEEE, 2019.
- [42] Pieter L Rijke. Lxxi. notice of a new method of causing a vibration of the air contained in a tube open at both ends. *The London, Edinburgh, and Dublin Philosophical Magazine and Journal of Science*, 17(116):419–422, 1859.
- [43] Jonathan P Epperlein, Bassam Bamieh, and Karl J Astrom. Thermoacoustics and the rijke tube: Experiments, identification, and modeling. *IEEE Control Systems Magazine*, 35(2):57–77, 2015.
- [44] GF Carrier. The mechanics of the rijke tube. *quarterly of Applied Mathematics*, 12(4):383–395, 1955.
- [45] AC McIntosh and S Rylands. A model of heat transfer in rijke tube burners. *Combustion science and technology*, 113(1):273–289, 1996.
- [46] JA Carvalho Jr, MA Ferreira, C Bressan, and JLG Ferreira. Definition of heater location to drive maximum amplitude acoustic oscillations in a rijke tube. *Combustion and Flame*, 76(1):17–27, 1989.
- [47] Jonas Pablo Moeck, Michael Oevermann, Rupert Klein, Christian Oliver Paschereit, and Heiko Schmidt. A two-way coupling for modeling thermoacoustic instabilities in a flat flame rijke tube. *Proceedings of the Combustion Institute*, 32(1):1199–1207, 2009.
- [48] Andrew C Noble, Galen B King, Normand M Laurendeau, James R Gord, and Sukesh Roy. Nonlinear thermoacoustic instability dynamics in a rijke tube. *Combustion Science and*

Technology, 184(3):293–322, 2012.

- [49] Lipika Kabiraj, RI Sujith, and Pankaj Wahi. Investigating the dynamics of combustion-driven oscillations leading to lean blowout. *Fluid Dynamics Research*, 44(3):031408, 2012.
- [50] Dan Zhao and ZH Chow. Thermoacoustic instability of a laminar premixed flame in a tube with a hydrodynamic region. *Journal of Sound and Vibration*, 332(14):3419–3437, 2013.
- [51] Yu Guan, Meenatchidevi Murugesan, and Larry KB Li. Strange nonchaotic and chaotic attractors in a self-excited thermoacoustic oscillator subjected to external periodic forcing. *Chaos: An Interdisciplinary Journal of Nonlinear Science*, 28(9):093109, 2018.
- [52] Lipika Kabiraj, Aditya Saurabh, Pankaj Wahi, and RI Sujith. Route to chaos for combustion instability in ducted laminar premixed flames. *Chaos: An Interdisciplinary Journal of Nonlinear Science*, 22(2):023129, 2012.
- [53] Praveen Kasthuri, Vishnu R Unni, and RI Sujith. Bursting and mixed mode oscillations during the transition to limit cycle oscillations in a matrix burner. *Chaos: An Interdisciplinary Journal of Nonlinear Science*, 29(4):043117, 2019.
- [54] Wyatt Culler, Xiaoling Chen, Stephen Peluso, Domenic Santavicca, Jacqueline O’Connor, and David Noble. Comparison of center nozzle staging to outer nozzle staging in a multi-flame combustor. In *Turbo expo: Power for land, sea, and air*, volume 51050, page V04AT04A024. American Society of Mechanical Engineers, 2018.
- [55] Jun Li, Yuantao Wang, Jinxing Chen, Junrui Shi, and Xueling Liu. Experimental study on standing wave regimes of premixed H₂–air combustion in planar micro-combustors partially filled with porous medium. *Fuel*, 167:98–105, 2016.
- [56] Guangyao Yang and Aiwu Fan. Experimental study on combustion characteristics of n-C₄H₁₀/air mixtures in a meso-scale tube partially filled with wire mesh. *Fuel*, 319:123783, 2022.
- [57] Haolin Yang, Sergey Minaev, Evgeniy Geynce, Hisashi Nakamura, and Kaoru Maruta. Filtration combustion of methane in high-porosity micro-fibrous media. *Combustion science and technology*, 181(4):654–669, 2009.
- [58] PJ Langhorne. Reheat buzz: an acoustically coupled combustion instability. part 1. experiment. *Journal of Fluid Mechanics*, 193:417–443, 1988.
- [59] YL Hardalupas and M Orain. Local measurements of the time-dependent heat release rate and equivalence ratio using chemiluminescent emission from a flame. *Combustion and*

Flame, 139(3):188–207, 2004.

- [60] Xianzhong Hu, Fangchao Bai, Chang Yu, and Fusheng Yan. Experimental study of the laminar flame speeds of the $\text{CH}_4/\text{H}_2/\text{CO}/\text{CO}_2/\text{N}_2$ mixture and kinetic simulation in oxygen-enriched air condition. *ACS omega*, 5(51):33372–33379, 2020.
- [61] Steven H Strogatz. *Nonlinear dynamics and chaos: with applications to physics, biology, chemistry, and engineering*. CRC press, 2018.
- [62] Matthew B Kennel, Reggie Brown, and Henry DI Abarbanel. Determining embedding dimension for phase-space reconstruction using a geometrical construction. *Physical review A*, 45(6):3403, 1992.
- [63] Arthur E Barnes. The calculation of instantaneous frequency and instantaneous bandwidth. *Geophysics*, 57(11):1520–1524, 1992.